International Journal of Plasticity 185 (2025) 104201

Contents lists available at ScienceDirect

International Journal of Plasticity

journal homepage: www.elsevier.com/locate/ijplas

A multi-physics model for the evolution of grain microstructure

I.T. Tandogan [a], M. Budnitzki [a,*], S. Sandfeld [a,b]

[a] Institute for Advanced Simulations – Materials Data Science and Informatics (IAS-9), Forschungszentrum Jülich GmbH, Jülich, 52425, Germany

[b] Chair of Materials Data Science and Materials Informatics, Faculty 5 – Georesources and Materials Engineering, RWTH Aachen University, Aachen, 52056, Germany

ARTICLE INFO

Keywords:
Crystal plasticity
Grain boundary migration
Microstructure evolution
Orientation phase field
Cosserat

ABSTRACT

When a metal is loaded mechanically at elevated temperatures, its grain microstructure evolves due to multiple physical mechanisms. Two of which are the curvature-driven migration of the grain boundaries due to increased mobility, and the formation of subgrains due to severe plastic deformation. Similar phenomena are observed during heat treatment subsequent to severe plastic deformation. Grain boundary migration and plastic deformation simultaneously change the lattice orientation at any given material point, which is challenging to simulate consistently. The majority of existing simulation approaches tackle this problem by applying separate, specialized models for mechanical deformation and grain boundary migration sequentially. Significant progress was made recognizing that the Cosserat continuum represents an ideal framework for the coupling between different mechanisms causing lattice reorientation, since rotations are native degrees of freedom in this setting.

In this work we propose and implement a multi-physics model, which couples Cosserat crystal plasticity to Henry–Mellenthin–Plapp (HMP) type orientation phase-field in a single thermodynamically consistent framework for microstructure evolution. Compared to models based on the Kobayashi–Warren–Carter (KWC) phase-field, the HMP formulation removes the nonphysical term linear in the gradient of orientation from the free energy density, thus eliminating long-range interactions between grain boundaries. Further, HMP orientation phase field can handle inclination-dependent grain boundary energies. We evaluate the model's predictions and numerical performance within a two-dimensional finite element framework, and compare it to a previously published results based on KWC phase-field coupled with Cosserat mechanics.

1. Introduction

Forming of metallic alloys involves deformation at elevated temperatures and heat treatment subsequent to severe plastic deformation, both of which extensively alter the granular microstructure and consequently the macroscopic material properties. The evolution of the polycrystalline structure comprised of grains of different sizes, shapes and orientations, and the corresponding grain boundary network can occur through multiple physical mechanisms including viscoplastic deformation, static and dynamic recrystallization, recovery, grain nucleation and growth (Rollett et al., 2017). Viscoplastic deformation changes the orientation of the crystal lattice, which can lead to the formation of localized slip and kink bands (Asaro and Rice, 1977; Marano et al., 2019) and the accompanied fragmentation of grains into sub-grains (Sedláček et al., 2002). Inside the grains dislocations build

* Corresponding author.
E-mail address: m.budnitzki@fz-juelich.de (M. Budnitzki).

https://doi.org/10.1016/j.ijplas.2024.104201
Received 2 August 2024; Received in revised form 29 October 2024
Available online 17 December 2024

up, often non-homogeneously, due to localized deformation and random trapping (Ashby, 1970). The resulting increase of energy is a driving force for the motion of grain boundaries, the mobility of which is related to misorientation between the grains (Gottstein and Shvindlerman, 2009). Grain boundary motion is possible via coordinated shuffling of atoms, which also reorients the crystal lattice. During recrystallization, grains tend to nucleate at locations of high misorientation, sites with high dislocation density and at second-phase particles, which then grow into the neighboring grains reducing the total energy.

These processes simultaneously change the lattice orientation at any given material point, which is challenging to simulate consistently. At atomistic length scale, molecular dynamics simulations were able to capture the complex physics of grain boundary deformation and motion (Mishin et al., 2010; Zhu et al., 2020; Chen et al., 2024). While they provide interesting insights, it is not feasible to apply them to the time and length scales of polycrystal evolution at mesoscale. Most of the mesoscale models treat the evolution mechanisms separately, covering either deformation or evolution of the grain structure. Classical crystal plasticity theories for bulk plasticity with fixed grain boundaries have been improved rigorously, and can accurately predict viscoplastic deformation in engineering problems (Roters et al., 2010), while generalized non-local theories make it possible to incorporate physical mechanisms such as size effects, strain localization and grain boundary dislocation interaction (Forest et al., 2000; Gurtin, 2000, 2008; Mayeur and McDowell, 2014; Yalçinkaya et al., 2021; Ryś et al., 2022; Forest and Ghiglione, 2023). Similarly, a more accurate continuum description of grain boundaries is possible with disclination and disconnection density based models (Sun et al., 2016, 2018; Joshi et al., 2022). The kinetics of grain boundary motion have been studied with a number of methods such as vertex techniques (cf. Soares et al., 1985; Gill and Cocks, 1996), cellular automata (e.g. Marx et al., 1999; Raabe, 2002), Monte-Carlo (Srolovitz, 1986; Rollett et al., 1992), level-set methods (Chen, 1995; Bernacki et al., 2008) and phase field models (Tourret et al., 2022), where the last two have the advantage of tracking the moving interface implicitly. The phase-field approaches for grain boundary migration are divided mainly into multi-phase field models (see Steinbach et al., 1996; Steinbach and Pezzolla, 1999; Fan and Chen, 1997) and orientation phase field models (cf. Kobayashi et al., 2000; Warren et al., 2003; Henry et al., 2012).

For the coupled evolution problem, the above mentioned independent methods have been combined mainly by employing them sequentially or through a phenomenological coupling. Usually, information is passed back and forth between a crystal plasticity (CP) model for deforming the structure and a model for grain boundary (GB) migration for evolving it, possibly with an intermediate step for the nucleation of grains based on stochastic methods or trigger criteria such as misorientation or stored energy. McElfresh and Marian (2023) used finite strain CP and a vertex model successively for static recrystallization and grain growth. Similarly, the cellular automata approach was combined with CP to model static (Sitko et al., 2020) and dynamic recrystallization (Popova et al., 2015; Li et al., 2016; Nagra et al., 2020), where Li et al. included mechanical feedback from cellular automata. Bernacki et al. (2011) and Sarrazola et al. (2020a,b) employed a level-set framework combined with CP, while Blesgen (2017) used higher order Cosserat CP in a staggered scheme. In a series of contributions, Takaki et al. (2009), Takaki and Tomita (2010), Takaki et al. (2014) developed models coupling multi-phase field with various deformation theories such as CP, strain gradient CP, Kocks–Mecking and J_2 models for static and dynamic recrystallization problems. Chen et al. (2015), Zhao et al. (2016) and Hu et al. (2021) efficiently simulated three dimensional static and dynamic recrystallization as well as deformation twinning in polycrystals by using spectral Fast-Fourier-Transform based multi-phase field and CP solvers. Abrivard et al. (2012) and Luan et al. (2020) coupled the KWC type orientation phase field extended with a stored dislocation energy term into finite element CP. Unlike multi-phase field, KWC has the advantage of representing lattice orientation as a degree of freedom. Mikula et al. (2019) coupled the grain orientation in the KWC model with the strain energy of a mechanically loaded elasto-plastic nanocrystalline system.

Although sequential combinations of different methods have been used successfully to model microstructure evolution along with deformation, several authors have sought a unified thermodynamically consistent field theory that strongly couples deformation and microstructure evolution. A class of sharp interface continuum models were developed, where shear loading can stimulate grain boundary motion (Cahn et al., 2006; Berbenni et al., 2013; Basak and Gupta, 2015). However, they are not tuned for the mesoscale, where interaction of bulk plasticity and grain boundaries is important. Recently, Bugas and Runnels (2024) proposed a novel reduced order multi-scale model to simulate plastic evolution of a microstructure, mediated through the shear-coupled motion of GBs. Admal et al. (2018) and He and Admal (2021) have proposed a model that considers bulk and grain boundary plasticity in unison. A large deformation strain gradient CP is formulated with a non-standard free energy density containing contributions from the full dislocation density tensor inspired by the KWC type orientation phase field. Hence, it is capable of predicting both shear-induced and curvature driven GB motion, grain sliding, rotation and subgrain nucleation, where the GB motion is accommodated by plastic slip process. Orientation phase field models are well suited for a strong coupling with crystal plasticity as the lattice orientation is a continuous field in the bulk and at the interface. Ask et al. (2018a,b, 2019, 2020) have combined the modified KWC orientation phase field of Abrivard et al. (2012) with Cosserat-type crystal plasticity with independent micro-rotation degrees of freedom, recognizing it as a natural framework for the coupling. Lattice orientation can evolve simultaneously due to viscoplastic deformation and GB migration, where the latter is driven by capillary forces as well as accumulated dislocation densities. The coupling of Cosserat continuum with orientation phase field allows heterogeneous reorientation and subgrain formation in the bulk. Recently, Ghiglione et al. (2024) showed through the torsion of a single crystal rod that the model can predict spontaneous grain nucleation in the presence of a lattice orientation gradient.

In the present work, a novel model inspired by the work of Ask et al. (2018a) is proposed where the Henry–Mellenthin–Plapp (HMP) type orientation phase field (Henry et al., 2012; Staublin et al., 2022) is strongly coupled with a Cosserat crystal plasticity (CCP) framework. This model offers several improvements. By design, the HMP model removes the non-physical long range interactions between the grain boundaries that exist in the KWC model due to the $|\nabla\theta|$ term in the free energy. Instead, the HMP model achieves localized grain boundaries using a singular coupling function. This coupling function can be modified in order to obtain the desired misorientation dependence of grain boundary energy without changing the variational form of the model,

e.g. for an inclination dependent energy. Moreover, the energy contribution of statistically stored dislocations (SSDs) to the free energy density, which was added by Abrivard et al. (2012) into the KWC model to drive GB motion, is modified. Originally this term altered the equilibrium value of the order parameter in the bulk, which is undesirable in a multi-phase context and breaks the singular coupling function in the HMP model. We propose a form that allows similar GB kinetics without changing the order parameter in the presence of dislocations.

This paper is structured as follows. Section 2 summarizes the general coupled orientation phase field and Cosserat CP framework, presents the governing equations and evolution of history variables in the proposed coupled model, and finishes by comparing it with the previous KWC+CCP framework by Ask et al. (2018a). Section 3 explores the fundamental mechanisms of the coupled model, establishing the model's parameters with simple numerical examples, namely, equilibrium profiles, shear loading and dislocation driven GB migration in a periodic bicrystal structure, as well as the triple junction test for curvature driven GB motion. Finally, the paper is concluded with a summary and an outlook in Section 4.

2. Model

This section presents the model framework, describing the kinematics, balance laws and the formulation of the constitutive laws within a small deformation setting. As a starting point Sections 2.1 and 2.2 give an overview of the coupled Cosserat-phase field model developed by Ask et al. (2018a) which was later modified slightly in Ask et al. (2018b), where Cosserat crystal plasticity was coupled with KWC type orientation phase field (Kobayashi et al., 2000; Warren et al., 2003). Section 2.3 proposes the Cosserat-HMP phase field model introducing a new free energy and some modifications, where we use a new phase field model for coupling (Henry et al., 2012; Staublin et al., 2022). Section 2.4 specifies the dissipation potential and presents the corresponding evolution equations for closure. Section 2.5 highlights the differences of the proposed model with the Cosserat-KWC phase field model of Ask et al. (2018a,b).

Notation

In the following, vectors a_i are denoted by $\underline{\boldsymbol{a}}$, 2nd order tensors A_{ij} by $\underset{\sim}{\boldsymbol{A}}$, the 3rd order Levi-Civita permutation tensor ϵ_{ijk} by $\underset{\approx}{\boldsymbol{\epsilon}}$, 4th order tensors C_{ijkl} by $\underset{\approx}{\boldsymbol{C}}$. The Kronecker delta is denoted by δ^{ij}. The gradient is denoted by $\nabla(.)$, divergence by $\nabla\cdot(.)$, transpose by $(.)^{\mathrm{T}}$, dot product by $(.)\cdot(.)$, double contraction by $(.):(.)$, and tensor product by $(.)\otimes(.)$. The transformation between pseudo-vector $\overset{\times}{\underline{\boldsymbol{a}}}$ and skew-symmetric tensor $\underset{\sim}{\boldsymbol{A}}^{\mathrm{skew}}$ is given by,

$$\overset{\times}{\underline{\boldsymbol{a}}} = \mathrm{axi}(\underset{\sim}{\boldsymbol{A}}^{\mathrm{skew}}) := -\frac{1}{2}\underset{\approx}{\boldsymbol{\epsilon}} : \underset{\sim}{\boldsymbol{A}}^{\mathrm{skew}} \quad \text{and} \quad \underset{\sim}{\boldsymbol{A}}^{\mathrm{skew}} = -\underset{\approx}{\boldsymbol{\epsilon}} \cdot \overset{\times}{\underline{\boldsymbol{a}}}. \tag{1}$$

2.1. Cosserat continuum coupled with orientation phase field

The Cosserat continuum introduces a microrotation tensor $\underset{\sim}{\boldsymbol{R}}$ which relates the current state of a triad of orthonormal directors to the initial state at each material point, independently from the displacements. In the small deformation setting, it is given by,

$$\underset{\sim}{\boldsymbol{R}} = \underset{\sim}{\boldsymbol{I}} - \underset{\approx}{\boldsymbol{\epsilon}} \cdot \underline{\boldsymbol{\Theta}} \tag{2}$$

where $\underset{\sim}{\boldsymbol{I}}$ is the identity tensor and $\underline{\boldsymbol{\Theta}}$ is the microrotation pseudo-vector. The displacement vector $\underline{\boldsymbol{u}}$ together with $\underline{\boldsymbol{\Theta}}$ describes the motion of a material point with six degrees of freedom. The objective deformation measures are given by Eringen and Kafadar (1976)

$$\underset{\sim}{\boldsymbol{e}} = \nabla\underline{\boldsymbol{u}} + \underset{\approx}{\boldsymbol{\epsilon}} \cdot \underline{\boldsymbol{\Theta}}, \qquad \underset{\sim}{\boldsymbol{\kappa}} = \nabla\underline{\boldsymbol{\Theta}}, \tag{3}$$

which are the deformation tensor and curvature tensor, respectively. The small deformation setting allows an additive decomposition of the strain into elastic and plastic contributions

$$\underset{\sim}{\boldsymbol{e}} = \underset{\sim}{\boldsymbol{e}}^{\mathrm{e}} + \underset{\sim}{\boldsymbol{e}}^{\mathrm{p}}, \tag{4}$$

where plastic curvature is not considered for simplicity. The rate of the deformation tensor can be expressed as

$$\dot{\underset{\sim}{\boldsymbol{e}}} = \dot{\underset{\sim}{\boldsymbol{\varepsilon}}} + \underset{\sim}{\boldsymbol{\omega}} + \underset{\approx}{\boldsymbol{\epsilon}} \cdot \dot{\underline{\boldsymbol{\Theta}}}, \tag{5}$$

where,

$$\dot{\underset{\sim}{\boldsymbol{\varepsilon}}} = \frac{1}{2}\left[\nabla\dot{\underline{\boldsymbol{u}}} + (\nabla\dot{\underline{\boldsymbol{u}}})^{\mathrm{T}}\right] \quad \text{and} \quad \underset{\sim}{\boldsymbol{\omega}} = \frac{1}{2}\left[\nabla\dot{\underline{\boldsymbol{u}}} - (\nabla\dot{\underline{\boldsymbol{u}}})^{\mathrm{T}}\right] \tag{6}$$

are the strain rate and spin tensors, respectively. The skew-symmetric part of $\dot{\underset{\sim}{\boldsymbol{e}}}$ can be represented by the pseudo-vector

$$\dot{\overset{\times}{\underline{\boldsymbol{e}}}} = \dot{\overset{\times}{\underline{\boldsymbol{\omega}}}} - \dot{\underline{\boldsymbol{\Theta}}}, \tag{7}$$

which relates the rotation of the material to the Cosserat microrotation. Using the elastic–plastic decomposition and defining plastic and elastic spin pseudo-vectors $\overset{\times}{\underline{\boldsymbol{\omega}}}^{\mathrm{p}} := \dot{\overset{\times}{\underline{\boldsymbol{e}}}}^{\mathrm{p}}$ and $\overset{\times}{\underline{\boldsymbol{\omega}}}^{\mathrm{e}} := \overset{\times}{\underline{\boldsymbol{\omega}}} - \overset{\times}{\underline{\boldsymbol{\omega}}}^{\mathrm{p}}$, respectively, we can write

$$\dot{\overset{\times}{\underline{\boldsymbol{e}}}}^{\mathrm{e}} = \dot{\overset{\times}{\underline{\boldsymbol{\omega}}}}^{\mathrm{e}} - \dot{\underline{\boldsymbol{\Theta}}}. \tag{8}$$

Eq. (8) expresses a link between the rotation rate of the crystal lattice and the Cosserat microrotation rate, which are distinct at this point. For our purposes they should be identical, which can be enforced by the internal constraint,

$$\overset{\times}{\underset{\sim}{e}}{}^{\mathrm{e}} \equiv 0, \tag{9}$$

which can be implemented on the constitutive level with a penalty parameter (Forest et al., 2000; Mayeur et al., 2011; Blesgen, 2014). Alternatively, a more sophisticated and efficient duality-based formulation was proposed recently by Baek et al. (2022).

In order to include grain boundary migration, the Cosserat theory is enhanced with an orientation phase field model. The latter defines the microstructure with the order parameter η, lattice orientation $\underline{\boldsymbol{\Theta}}$ and their gradients $\nabla\eta$ and $\nabla\underline{\boldsymbol{\Theta}}$. The order parameter $\eta \in [0,1]$ is a coarse-grained measure of crystalline order that takes the value $\eta = 1$ in the bulk of the grain and $\eta < 1$ in the diffuse grain boundaries. The coupling of Cosserat continuum with the phase field is explained below.

2.2. Balance laws

In order to derive a consistent set of balance equations and boundary conditions, the principle of virtual power is applied using following set of virtual rates

$$\mathcal{V} = \left\{ \dot{\eta}^\star, \nabla\dot{\eta}^\star, \underline{\dot{u}}^\star, \nabla\underline{\dot{u}}^\star, \underline{\dot{\Theta}}^\star, \nabla\underline{\dot{\Theta}}^\star \right\}. \tag{10}$$

The reader is referred to Ask et al. (2018a) for the detailed derivation steps. The resulting balance equations and boundary conditions are given by,

$$\nabla \cdot \underline{\boldsymbol{\xi}}_\eta + \pi_\eta + \pi_\eta^{\mathrm{ext}} = 0 \qquad \text{in } \Omega, \tag{11}$$

$$\nabla \cdot \underset{\sim}{\boldsymbol{\sigma}} + \underline{\boldsymbol{f}}^{\mathrm{ext}} = \underline{\mathbf{0}} \qquad \text{in } \Omega, \tag{12}$$

$$\nabla \cdot \underset{\sim}{\boldsymbol{m}} + 2\overset{\times}{\underset{\sim}{\sigma}} + \underline{\boldsymbol{c}}^{\mathrm{ext}} = \underline{\mathbf{0}} \qquad \text{in } \Omega, \tag{13}$$

$$\underline{\boldsymbol{\xi}}_\eta \cdot \underline{\boldsymbol{n}} = \pi_\eta^{\mathrm{c}} \qquad \text{on } \partial\Omega, \tag{14}$$

$$\underset{\sim}{\boldsymbol{\sigma}} \cdot \underline{\boldsymbol{n}} = \underline{\boldsymbol{f}}^{\mathrm{c}} \qquad \text{on } \partial\Omega, \tag{15}$$

$$\underset{\sim}{\boldsymbol{m}} \cdot \underline{\boldsymbol{n}} = \underline{\boldsymbol{c}}^{\mathrm{c}} \qquad \text{on } \partial\Omega, \tag{16}$$

where $\underline{\boldsymbol{f}}$ and $\underline{\boldsymbol{c}}$ are forces and couples, respectively. The superscript $(.)^{\mathrm{ext}}$ denotes external body forces and couples, while $(.)^{\mathrm{c}}$ denotes contact forces and couples. The outward normal to the surface $\partial\Omega$ of the volume Ω is $\underline{\boldsymbol{n}}$. The generalized stresses π_η and $\underline{\boldsymbol{\xi}}_\eta$ correspond to Gurtin's microforces (Gurtin, 1996) and are conjugate to the order parameter η and its gradient $\nabla\eta$. The stress $\underset{\sim}{\boldsymbol{\sigma}}$ (which is not symmetric) is conjugate to the Cosserat deformation $\underset{\sim}{\boldsymbol{e}}$. The couple-stress $\underset{\sim}{\boldsymbol{m}}$ is conjugate to the curvature $\underset{\sim}{\boldsymbol{\kappa}}$. Eqs. (11), (12) and (13) represent balance of generalized stresses, balance of linear momentum and balance of angular momentum, respectively.

2.3. Free energy density and constitutive equations

We assume that the Helmholtz free energy density Ψ is defined as

$$\rho\Psi := \psi\left(\eta, \nabla\eta, \underset{\sim}{\boldsymbol{e}}^{\mathrm{e}}, \underset{\sim}{\boldsymbol{\kappa}}, r_\alpha\right) \tag{17}$$

where r_α are internal variables related to plasticity. Applying the Clausius-Duhem inequality results in

$$-\left[\pi_\eta + \frac{\partial\psi}{\partial\eta}\right]\dot{\eta} + \left[\underline{\boldsymbol{\xi}}_\eta - \frac{\partial\psi}{\partial\nabla\eta}\right] \cdot \nabla\dot{\eta} + \left[\underset{\sim}{\boldsymbol{\sigma}} - \frac{\partial\psi}{\partial\underset{\sim}{\boldsymbol{e}}^{\mathrm{e}}}\right] : \dot{\underset{\sim}{\boldsymbol{e}}}^{\mathrm{e}} + \left[\underset{\sim}{\boldsymbol{m}} - \frac{\partial\psi}{\partial\underset{\sim}{\boldsymbol{\kappa}}}\right] : \dot{\underset{\sim}{\boldsymbol{\kappa}}} + \underset{\sim}{\boldsymbol{\sigma}} : \dot{\underset{\sim}{\boldsymbol{e}}}^{\mathrm{p}} - \sum_\alpha \frac{\partial\psi}{\partial r_\alpha}\dot{r}_\alpha \geq 0. \tag{18}$$

In order to recover the relaxation behavior of the phase field model, the stress π_η is assumed to contain energetic and dissipative contributions such that

$$\pi_\eta = \pi_\eta^{\mathrm{eq}} + \pi_\eta^{\mathrm{dis}}. \tag{19}$$

Then, the constitutive relations are given by

$$\pi_\eta^{\mathrm{eq}} = -\frac{\partial\psi}{\partial\eta}, \qquad \underline{\boldsymbol{\xi}}_\eta = \frac{\partial\psi}{\partial\nabla\eta}, \qquad \underset{\sim}{\boldsymbol{\sigma}} = \frac{\partial\psi}{\partial\underset{\sim}{\boldsymbol{e}}^{\mathrm{e}}}, \qquad \underset{\sim}{\boldsymbol{m}} = \frac{\partial\psi}{\partial\underset{\sim}{\boldsymbol{\kappa}}}. \tag{20}$$

For the coupled problem, a general form of free energy functional, including phase field variables and deformation measures, is considered:

$$\begin{aligned}\psi\left(\eta, \nabla\eta, \underset{\sim}{\boldsymbol{e}}^{\mathrm{e}}, \underset{\sim}{\boldsymbol{\kappa}}, r_\alpha\right) = f_0 \left[\alpha V(\eta) + \frac{\nu^2}{2}|\nabla\eta|^2 + \mu^2 g(\eta) a^2(\underline{\boldsymbol{n}}, \underline{\boldsymbol{\Theta}}) \|\underset{\sim}{\boldsymbol{\kappa}}\|^2\right] \\ + \frac{1}{2}\underset{\sim}{\boldsymbol{\varepsilon}}^{\mathrm{e}} : \underset{\approx}{\boldsymbol{E}}^{\mathrm{s}} : \underset{\sim}{\boldsymbol{\varepsilon}}^{\mathrm{e}} + 2\mu_{\mathrm{c}}(\eta)\overset{\times}{\underset{\sim}{\boldsymbol{e}}}{}^{\mathrm{e}} \cdot \underset{\sim}{\boldsymbol{e}}^{\mathrm{e}} + \phi(\eta)\sum_{\alpha=1}^{N}\frac{\lambda}{2}\mu^{\mathrm{e}} r_\alpha^2.\end{aligned} \tag{21}$$

The first line of (21) is a generalization of the Henry–Mellenthin–Plapp free energy (Henry et al., 2012) to three dimensions and scaled with the normalization parameter f_0 with unit J/m^3. The potential $V(\eta)$ penalizes the existence of grain boundaries, where

$\eta < 1$, and depending on whether it is a double-well or single-well potential, it is possible to have solid and liquid phases or solid phase only. For our purposes, we choose a single-well potential in analogy to the one used by Staublin et al. (2022). The second and third terms are grain boundary contributions in terms of the order parameter η and the lattice curvature $\underset{\sim}{\kappa}$, penalizing gradients in η and $\underline{\Theta}$, respectively, where the coefficients ν and μ with unit m and the non-dimensional α set the length scale of the diffuse grain boundary. Localized grain boundary solutions are made possible by the third term through $g(\eta)$, the singular coupling function that tends to infinity as $\eta \to 1$, relating lattice orientation to the phase field. The anisotropy coefficient $a(\underline{n}, \underline{\Theta})$ can be used to introduce an inclination dependence of the grain boundary energy, where $\underline{n}$ is the grain boundary normal (Staublin et al., 2022). A similar dependence within the KWC model is only possible through modified formulations (Admal et al., 2019; Kim et al., 2021).

The second line of (21) contains the energy contribution due to symmetric and skew-symmetric elastic deformation, where $\underset{\approx}{\boldsymbol{E}}^{\mathrm{s}}$ is the 4th order elasticity tensor and $\mu_{\mathrm{c}}(\eta)$ is the Cosserat couple modulus which can potentially have different values depending on order parameter. If μ_{c} is sufficiently large, the skew-symmetric part of the deformation is penalized, which enforces the constraint (9); then the Cosserat microrotation follows the lattice orientation. The last term is the energy contribution due to accumulated dislocations, where N is the number of slip systems, λ is a parameter close to 0.3 (Hirth et al., 1983), μ^{e} is the shear modulus and r_α are internal variables associated with SSDs. $\phi(\eta)$ is a coupling function depending on the order parameter, which allows SSDs to act as a driving force for the migration of grain boundaries.

Restricting the problem to two dimensions allows a considerable simplification of the equations. In 2D, microrotations reduce to $\underline{\Theta} = [0\ 0\ \theta]^{\mathrm{T}}$, hence it follows that $\overset{\times}{\underline{\omega}} = \left[0\ 0\ \overset{\times}{\omega}\right]^{\mathrm{T}}$ and $\overset{\times}{\underline{e}} = \left[0\ 0\ \overset{\times}{e}\right]^{\mathrm{T}}$. Similarly, the couple-stress $\underset{\sim}{\boldsymbol{m}}$ reduces to $\underline{\boldsymbol{m}}_\theta = [m_{31}\ m_{32}\ m_{33}]^{\mathrm{T}}$. Further, assuming an isotropic grain boundary energy and constant μ_{c}, Eq. (21) simplifies to

$$\begin{aligned}\psi\left(\eta, \nabla\eta, \underset{\sim}{\boldsymbol{\varepsilon}}^{\mathrm{e}}, \nabla\theta, r_\alpha\right) = f_0\left[\alpha V(\eta) + \frac{\nu^2}{2}|\nabla\eta|^2 + \mu^2 g(\eta)|\nabla\theta|^2\right] \\ + \frac{1}{2}\underset{\sim}{\boldsymbol{\varepsilon}}^{\mathrm{e}} : \underset{\approx}{\boldsymbol{E}}^{\mathrm{s}} : \underset{\sim}{\boldsymbol{\varepsilon}}^{\mathrm{e}} + 2\mu_{\mathrm{c}}\left(\overset{\times}{e}^{\mathrm{e}}\right)^2 + \phi(\eta)\sum_{\alpha=1}^{N}\frac{\lambda}{2}\mu^{\mathrm{e}} r_\alpha^2.\end{aligned} \tag{22}$$

Inserting the free energy (22) into (20), we obtain the state laws

$$\pi_\eta^{\mathrm{eq}} = -f_0\left[\alpha V_{,\eta} + \mu^2 g_{,\eta}|\nabla\theta|^2\right] - \phi_{,\eta}\sum_{\alpha=1}^{N}\frac{\lambda}{2}\mu^{\mathrm{e}} r_\alpha^2, \tag{23}$$

$$\underset{\sim}{\boldsymbol{\xi}}_\eta = f_0\left[\nu^2\nabla\eta\right], \tag{24}$$

$$\underline{\boldsymbol{m}}_\theta = f_0\left[2\mu^2 g(\eta)\nabla\theta\right], \tag{25}$$

$$\underset{\sim}{\boldsymbol{\sigma}} = \underset{\approx}{\boldsymbol{E}}^{\mathrm{s}} : \underset{\sim}{\boldsymbol{\varepsilon}}^{\mathrm{e}} - 2\mu_{\mathrm{c}}\,\underset{\sim}{\boldsymbol{\epsilon}} \cdot \underset{\sim}{\overset{\times}{\boldsymbol{e}}}^{\mathrm{e}}, \tag{26}$$

where $(.)_{,\eta}$ denotes partial derivative w.r.t. the order parameter η. The last term in (26) is the skew part of the stress tensor and it is equivalent to $\overset{\times}{\underline{\sigma}} = 2\mu_{\mathrm{c}}\,\overset{\times}{\underline{e}}^{\mathrm{e}}$, or $\overset{\times}{\sigma} = 2\mu_{\mathrm{c}}\,\overset{\times}{e}^{\mathrm{e}}$ in 2D.

2.4. Dissipation potential and evolution equations

The formulation of the evolution equations are slightly different between Ask et al. (2018a) and Ask et al. (2018b) in their treatment of the dissipation potential and an eigen-deformation term. Firstly, in the second publication the dissipative contribution to the stress $\underset{\sim}{\sigma}$ is dropped. Previously, this resulted in a separate evolution term of Θ similar to the phase field model, which becomes redundant in the coupled model. Secondly, the eigen-deformation is considered as a part of plastic deformation rather than as a separate strain, whose function is explained below. This work follows the approach of Ask et al. (2018b) summarized in the following.

The dissipation potential Ω is assumed to contain two separate contributions in terms of $\underset{\sim}{\boldsymbol{\sigma}}$, R_α and π_η^{dis}

$$\Omega = \Omega^{\mathrm{p}}(\underset{\sim}{\boldsymbol{\sigma}}, R_\alpha; \eta) + \Omega^{\eta}(\pi_\eta^{\mathrm{dis}}), \tag{27}$$

where

$$R_\alpha = \frac{\partial\psi}{\partial r_\alpha} \tag{28}$$

are thermodynamic forces related to r_α. The plastic flow, hardening rules, and evolution equations are obtained from Ω as

$$\underset{\sim}{\dot{\boldsymbol{\varepsilon}}}^{\mathrm{p}} = \frac{\partial\Omega^{\mathrm{p}}}{\partial\underset{\sim}{\boldsymbol{\sigma}}}, \qquad \dot{r}_\alpha = -\frac{\partial\Omega^{\mathrm{p}}}{\partial R_\alpha}, \qquad \dot{\eta} = -\frac{\partial\Omega^{\eta}}{\partial\pi_\eta^{\mathrm{dis}}}. \tag{29}$$

The plastic deformation mechanism is implemented through a Cosserat crystal plasticity framework. The plastic dissipation potential is chosen as,

$$\Omega^{\mathrm{p}}(\underset{\sim}{\boldsymbol{\sigma}}, R_\alpha; \eta) = \sum_{\alpha=1}^{N}\frac{K_{\mathrm{v}}}{n+1}\left\langle\frac{|\tau^\alpha| - R_\alpha/\phi(\eta)}{K_{\mathrm{v}}}\right\rangle^{n+1} + \frac{1}{2}\tau_*^{-1}(\eta)\,\underset{\sim}{\overset{\times}{\boldsymbol{\sigma}}} \cdot \underset{\sim}{\overset{\times}{\boldsymbol{\sigma}}}, \tag{30}$$

where $\langle\cdot\rangle$ are Macaulay brackets defined by $\langle\cdot\rangle := \max(0, \cdot)$, K_{v} and n are viscosity parameters, τ^α is the resolved shear stress, and R_α is the critical resolved shear stress of slip system α. While the first term in (30) is standard, the second term is included to account for atomic reshuffling happening at the grain boundaries during migration and resulting in reorientation (Ask et al., 2018b), which

is a purely skew-symmetric contribution acting only on the plastic spin. It is supposed be active only in the grain boundary region, which is implemented by introducing an inverse mobility function $\tau_*(\eta)$ that is chosen to be small inside grain boundary and large in bulk. Its explicit form is given in Section 2.5. From the free energy functional we have,

$$R_\alpha = \frac{\partial \psi}{\partial r_\alpha} = \lambda \phi(\eta) \mu^{\mathrm{e}} r_\alpha = \lambda \phi(\eta) \mu^{\mathrm{e}} b \sqrt{\sum_{\beta=1}^{N} h^{\alpha\beta} \rho^\beta}, \tag{31}$$

where the internal variables r_α are related to the SSD densities ρ^α as

$$r_\alpha = b \sqrt{\sum_{\beta=1}^{N} h^{\alpha\beta} \rho^\beta}. \tag{32}$$

The parameter b is the norm of the Burgers vector of the considered slip system family and $h^{\alpha\beta}$ is the slip system interaction matrix. The resolved shear stress τ^α is the projection of stress $\underset{\sim}{\sigma}$ on slip system α

$$\tau^\alpha = \underline{l}^\alpha \cdot \underset{\sim}{\sigma} \cdot \underline{n}^\alpha, \tag{33}$$

where $\underline{l}^\alpha$ is the slip direction and $\underline{n}^\alpha$ is the slip plane normal. Since in the Cosserat framework the stress tensor is generally non-symmetric, the skew part contributes an additional term to the resolved shear stress which can considered to be a size dependent kinematic hardening (Forest, 2008). Substituting (30) into (29), we get the evolution of plastic deformation

$$\underset{\sim}{\dot{e}}^{\mathrm{p}} = \sum_{\alpha=1}^{N} \dot{\gamma}^\alpha \underline{l}^\alpha \otimes \underline{n}^\alpha + \frac{1}{2} \tau_*^{-1}(\eta) \mathrm{skew}(\underset{\sim}{\sigma}), \tag{34}$$

with

$$\dot{\gamma}^\alpha = \left\langle \frac{|\tau^\alpha| - R_\alpha/\phi(\eta)}{K_{\mathrm{v}}} \right\rangle^n \mathrm{sign}\, \tau^\alpha \tag{35}$$

as the slip rate according to the viscoplastic flow rule from Cailletaud (1992). We can write

$$\overset{\times}{\underline{e}}^{\mathrm{p}} = \overset{\times}{\underline{e}}^{\mathrm{slip}} + \overset{\times}{\underline{e}}^*, \tag{36}$$

where

$$\overset{\times}{\underline{e}}^{\mathrm{slip}} = \overset{\times}{\underline{\omega}}^{\mathrm{p}} - \overset{\times}{\underline{\omega}}^*, \qquad \underset{\sim}{\omega}^{\mathrm{p}} - \underset{\sim}{\omega}^* = \mathrm{skew}\left(\sum_{\alpha=1}^{N} \dot{\gamma}^\alpha \underline{l}^\alpha \otimes \underline{n}^\alpha \right), \tag{37}$$

$$\overset{\times}{\underline{e}}^* = \overset{\times}{\underline{\omega}}^*, \qquad \overset{\times}{\underline{\omega}}^* = \tau_*^{-1}(\eta) \overset{\times}{\underline{\sigma}}. \tag{38}$$

The eigenrotation $\overset{\times}{\underline{e}}^*$ is introduced to make sure that initial stresses in a polycrystal composed of grains with different orientations are zero. Consider, the elastic skew-symmetric deformation

$$\overset{\times}{\underline{e}}^{\mathrm{e}} = \mathrm{axi}(\mathrm{skew}[\nabla u]) - \overset{\times}{\underline{e}}^{\mathrm{p}} - \underline{\Theta} = \mathrm{axi}(\mathrm{skew}[\nabla u]) - \overset{\times}{\underline{e}}^{\mathrm{slip}} - \overset{\times}{\underline{e}}^* - \underline{\Theta}. \tag{39}$$

If the Cosserat microrotation represents the lattice orientation and the initial total deformation is assumed to be zero, clearly elastic deformation is non-zero, unless we set,

$$\overset{\times}{\underline{e}}^*(t=0) = \overset{\times}{\underline{e}}^{\mathrm{p}}(t=0) = -\underline{\Theta}(t=0). \tag{40}$$

This non-zero initial condition of plastic slip is adopted following Admal et al. (2018) and Ask et al. (2018b). From (39), it is seen that a moving grain boundary results in non-zero $\overset{\times}{\underline{e}}^{\mathrm{e}}$ and $\overset{\times}{\underline{\sigma}}$ in the region of the moving front, which are relaxed by the evolution of $\overset{\times}{\underline{e}}^*$ in (38).

During plastic deformation, the SSD density evolves by multiplication and annihilation mechanisms following a modified Kocks–Mecking–Teodosiu law (Abrivard et al., 2012; Ask et al., 2018a,b), such that

$$\dot{\rho}^\alpha = \begin{cases} \frac{1}{b}\left(K \sqrt{\sum_\beta a^{\alpha\beta} \rho^\beta} - 2d\rho^\alpha \right) |\dot{\gamma}| - \rho^\alpha C_{\mathrm{D}} A(|\nabla\theta|) \dot{\eta} & \text{if} \quad \dot{\eta} > 0 \\ \frac{1}{b}\left(K \sqrt{\sum_\beta a^{\alpha\beta} \rho^\beta} - 2d\rho^\alpha \right) |\dot{\gamma}| & \text{if} \quad \dot{\eta} \le 0, \end{cases} \tag{41}$$

where the extra term in the first line accounts for the static recovery of dislocations in the wake of a sweeping grain boundary (Abrivard et al., 2012; Ask et al., 2018a; Bailey and Hirsch, 1962). K is the mobility constant, d is the critical annihilation distance between dislocations of opposite sign, and $a^{\alpha\beta}$ is an interaction matrix for cross-slip. Either partial recovery, or in the case of sufficiently high values of C_{D}, full recovery in the wake is achieved, and the function $A(|\nabla\theta|) = \tanh(C_{\mathrm{A}}^2 |\nabla\theta|^2)$ localizes this recovery to the grain boundary region, where C_{A} has unit m. This is a simplistic representation of the combined absorption and annihilation recovery mechanisms that occur during the migration of a grain boundary. The evolution of the order parameter η is governed by the quadratic dissipation potential

$$\Omega^\eta = \frac{1}{2} \tau_\eta^{-1} (\pi_\eta^{\mathrm{dis}})^2 \tag{42}$$

chosen in analogy to Gurtin (1996) and Abrivard et al. (2012), where $\tau_\eta(\eta, \nabla\eta, \nabla\theta, T)$ is a positive scalar function. Applying (29) we get

$$\pi_\eta^{\text{dis}} = -\tau_\eta \dot{\eta}. \tag{43}$$

Inserting (23)–(25) and (43) into the balance laws (11) and (13), while assuming vanishing body forces and couples forces, gives the governing equations for the order parameter η and lattice orientation θ:

$$\tau_\eta \dot{\eta} = f_0 \nu^2 \nabla^2 \eta - f_0 \left[\alpha V_{,\eta} + \mu^2 g_{,\eta} |\nabla\theta|^2\right] - \phi_{,\eta} \sum_{\alpha=1}^{N} \frac{\lambda}{2} \mu^{\text{e}} r_\alpha^2 \tag{44}$$

$$0 = f_0 \nabla \cdot \left[\mu^2 g(\eta) \nabla\theta\right] + 2\mu_{\text{c}} \overset{\times}{\underset{\sim}{e}}{}^{\text{e}} \tag{45}$$

where the differences from Ask et al. (2018a,b, 2019) are highlighted by the gray box to be discussed in Section 2.5. Eq. (45) can be rewritten using (38) as

$$-\tau_*(\eta) \overset{\times}{\underset{\sim}{e}}{}^{*} = f_0 \nabla \cdot \left[\mu^2 g(\eta) \nabla\theta\right]. \tag{46}$$

Setting $\mu_{\text{c}} = 0$ recovers the HMP evolution equations [cf. Henry et al., 2012; Staublin et al., 2022] without θ relaxation and with the addition of an SSD term.

In the free energies (21) or (22), the choice of potential $V(\eta)$ and singular coupling function $g(\eta)$ of the phase field model requires some care as described by Henry et al. (2012) and Staublin et al. (2022). The following conditions must be met:

1. The value of the potential in the bulk of the grain is $V(1) = 0$
2. 1 is a minimum: $V'(1) = 0$
3. The potential should have only one single minimum: $V''(\eta) > 0$ for all η.
4. To enable a uniformly strained solid (small constant $\nabla\theta$) to be stable against the spontaneous formation of grain boundaries, we follow Henry et al. (2012), and impose the constraint $9V''(1) > V'''(1)$ when the coupling function $g(\eta) \sim (1-\eta)^{-2}$. This condition is irrelevant if we choose $g(\eta) \sim (1-\eta)^{-3}$ and thus this divergence of $g(\eta)$ stabilizes localized boundaries against uniform strain regardless. This condition should be reconsidered if a different $g(\eta)$ is used.

We choose a simple second order single-well potential $V(\eta)$ satisfying the above conditions

$$V(\eta) = \frac{1}{2}(1-\eta)^2 \tag{47}$$

and adopt the singular coupling function in Staublin et al. (2022)

$$g(\eta) = \frac{7\eta^3 - 6\eta^4}{(1-\eta)^3}. \tag{48}$$

2.5. Comparison with KWC+CCP

The main form of the free energy density and the governing equations proposed by Ask et al. (2018b, 2019) are as follows,

$$\begin{aligned} \psi^{\text{KWC+CCP}}\left(\eta, \nabla\eta, \underset{\sim}{\boldsymbol{e}}^{\text{e}}, \nabla\theta, r_\alpha\right) = f_0 \left[V(\eta) + \frac{\nu^2}{2}|\nabla\eta|^2 + sg^*(\eta)|\nabla\theta| + \frac{\epsilon^2}{2} h^*(\eta) |\nabla\theta|^2\right] \\ + \frac{1}{2} \underset{\sim}{\boldsymbol{\varepsilon}}^{\text{e}} : \underset{\approx}{\boldsymbol{E}}^{\text{s}} : \underset{\sim}{\boldsymbol{\varepsilon}}^{\text{e}} + 2\mu_{\text{c}} \left(\overset{\times}{\underset{\sim}{e}}{}^{\text{e}}\right)^2 + \eta \sum_{\alpha=1}^{N} \frac{\lambda}{2} \mu^{\text{e}} r_\alpha^2, \end{aligned} \tag{49}$$

$$\tau_\eta \dot{\eta} = f_0 \nu^2 \nabla^2 \eta - f_0 \left[V_{,\eta} + sg^*_{,\eta} |\nabla\theta| + \frac{\epsilon^2}{2} h^*_{,\eta} |\nabla\theta|^2\right] - 1 \sum_{\alpha=1}^{N} \frac{\lambda}{2} \mu^{\text{e}} r_\alpha^2, \tag{50}$$

$$0 = \frac{f_0}{2} \nabla \cdot \left[sg^*(\eta) \frac{\nabla\theta}{|\nabla\theta|} + \epsilon^2 h^*(\eta) \nabla\theta\right] + 2\mu_{\text{c}} \overset{\times}{\underset{\sim}{e}}{}^{\text{e}}, \tag{51}$$

where the main differences as compared to the proposed HMP+CCP Eqs. (44) and (45) are highlighted. The most significant difference, stemming from usage of different orientation phase field models, is the existence of the linear $|\nabla\theta|$ term in (50) and the corresponding singular term in (51). This term is necessary in KWC and responsible for the localization of grain boundaries as it is penalizing solutions with uniform gradient of orientation. However, as it is singular inside the grains, it requires regularization during the numerical solution (Kobayashi et al., 2000; Warren et al., 2003). Moreover, the singular diffusion equation allows long-range interactions between grain boundaries, which results in a rotation rate for grains independent on the distance between grain boundaries (Kobayashi and Giga, 1999). Hence, the only way to prevent unwanted grain rotations in the KWC model is to use a mobility function that takes small values inside the grain (Warren et al., 2003). On the other hand, the HMP model omits the linear $|\nabla\theta|$ term in free energy, and instead uses a singular coupling function $g(\eta)$ which approaches infinity inside the grains. As a consequence, it has local interaction of grain boundaries and a constant mobility is sufficient to suppress grain rotations (Henry et al., 2012).

Table 1
Parameter set used for the coupled Cosserat Crystal Plasticity - HMP orientation phase field model.

Phase field	f_0	t_0	τ_η	$\hat{\tau}_*$	ν	α	μ
	87 kPa	1 s	$0.1 f_0 t_0$	$1 f_0 t_0$	1 μm	150	$2.5/\pi$ μm
Mechanics	C_{11}	C_{12}	C_{44}	μ_c	λ	b	C_A
	160 GPa	110 GPa	75 GPa	750 GPa	0.3	0.2556 nm	$\sqrt{10}$ μm
	K_v	n	K	d	$h^{\alpha\beta}$	$a^{\alpha\beta}$	C_D
	10 MPa $s^{1/n}$	10	0.1	10 nm	$\delta^{\alpha\beta}$	$\delta^{\alpha\beta}$	100

Another difference is the way the atomic reshuffling process, i.e. the term $\tau_*(\eta)\overset{\times}{e}^*$ in (46), is localized to the grain boundaries. In the series of papers on the KWC+CCP model, Ask et al. (2018a, 2019, 2020) have used various forms such as

$$\tau_* = \hat{\tau}_* \tanh^{-1}(C_*^2|\nabla\eta|^2), \quad \tau_* = \hat{\tau}_* \tanh^{-1}(C_*^2|\nabla\theta|^2), \quad \tau_* = \hat{\tau}_* \left(1 - \left[1 - \frac{\mu_p}{\varepsilon}\right] \exp(-\beta_p \varepsilon |\nabla\theta|)\right), \tag{52}$$

all of which are large in the bulk of grain and small at the grain boundary, with slightly different dynamics. In the proposed HMP+CCP model such a function already naturally exists, i.e. the singular coupling function $g(\eta)$. Hence, we propose

$$\tau_* = \hat{\tau}_* g(\eta). \tag{53}$$

Looking at Eq. (46), using (53) can be interpreted as a translation of the idea proposed by Korbuly et al. (2017) to the coupled model, where they modify their mobility coefficient related to $\dot{\theta}$ in the same way in order to counterbalance the divergence of $g(\eta)$ multiplying $\nabla\theta$ in (45). This modification significantly improves the convergence behavior of the model; we explore its implications for the Cosserat mechanics.

Finally, a modification of the SSD energy term in (44) or (50) is proposed. In the work of Ask et al. (2018a), the multiplier function $\phi(\eta)$ [cf. Eq. (22)] is $\phi(\eta) = \eta$, resulting in $\phi_{,\eta}(\eta) = 1$. This has an important consequence on the equilibrium value of the order parameter inside the grains, when the dislocation density ρ^α is non-zero. We can easily calculate it from (44) or (50). At equilibrium, the gradient terms inside the grain and the rate term are zero, so we have

$$0 = f_0 \alpha (1 - \eta^{\mathrm{eq}}) - \phi_{,\eta}(\eta^{\mathrm{eq}}) \sum_{\alpha=1}^{N} \frac{\lambda}{2} \mu^{\mathrm{e}} r_\alpha^2, \tag{54}$$

or

$$\eta^{\mathrm{eq}} = 1 - \frac{\phi_{,\eta}(\eta^{\mathrm{eq}}) \sum_{\alpha=1}^{N} \frac{\lambda}{2} \mu^{\mathrm{e}} b^2 \sum_{\beta=1}^{N} h^{\alpha\beta} \rho^\beta}{f_0 \alpha}. \tag{55}$$

It is clear that, when $\phi_{,\eta} = 1$, the equilibrium value of the order parameter η^{eq} becomes less then 1, which is a change compared to the pure phase field model (Abrivard et al., 2012; Ask et al., 2018a). This is a significant problem for the formulation of the HMP phase field, since the model relies on the singularity of $g(\eta)$ inside the grains. We believe this could also be problematic if more complex potentials $V(\eta)$ with temperature dependence and minima for different phases are considered. In (55), it can be seen that if the derivative of $\phi(\eta)$ is taken to be zero inside the grain, i.e. $\phi_{,\eta}(\eta = 1) = 0$, then $\eta^{\mathrm{eq}} = 1$ independent of the SSD density. However, since this term is also the driving force for grain boundary migration due to dislocations, the choice of the function affects the grain boundary velocity. We have explored several polynomial forms and concluded that some of them can fit our purpose without modifying the dynamics considerably, which is discussed in Section 3 below.

3. Numerical examples

In this section, the proposed model and its capabilities are tested through numerical examples simulated with the finite element method and the results are discussed. The geometry shown in Fig. 1 is used to examine equilibrium profiles at the grain boundaries, elastic shear loading and grain boundary migration due to stored dislocation density. The classical triple-junction problem for testing phase field models, shown in Fig. 6, is used to confirm our numerical implementation. Finally, the setup in Fig. 1 is used again to simulate a scenario with plastic deformation and grain boundary migration.

For these examples we consider the two dimensional form of the model governed by Eqs. (44), (12) and (45). The external body forces and couple forces as well as the contact forces and couples in Eqs. (11)–(16) are assumed to be zero. Plane strain conditions are assumed. We use isotropic grain boundary energies for simplicity, and focus on the mechanisms made possible by the Cosserat coupling. The simulated material is pure copper (Cu), although we do not pursue a rigorous fitting to experimental data at this stage; instead the model parameters are chosen to be in a reasonable range [see e.g. Tschopp et al., 2015 and Ask et al., 2019]. As presented in Appendix A, the asymptotic analysis for the HMP phase field can also be used for the coupled model to obtain equilibrium profiles and the isotropic grain boundary energy for given misorientations. The parameters are calibrated to have 0.5 J/m^2 grain boundary energy at a 15° misorientation. Unless otherwise mentioned, the model parameters given in Table 1 are used in the simulations.

The model has been implemented in the FEniCS 2019 open-source finite element library (Alnaes et al., 2015) used together with the MFront code generator for the material models (Helfer et al., 2015). FEniCS handles the finite element framework and the global Newton–Raphson procedure, while MFront is responsible for the constitutive portion of the model and iterations at the integration

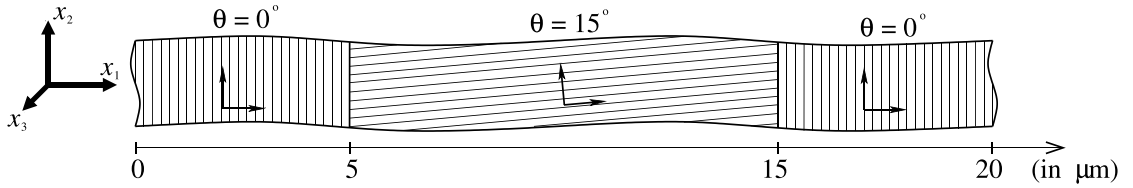

Fig. 1. Representative periodic bicrystal structure with variation in x_1 direction.

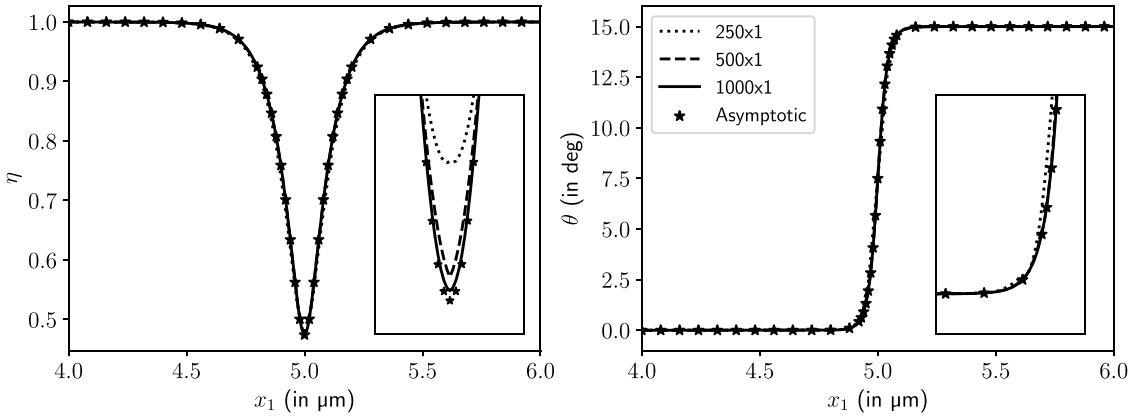

Fig. 2. Equilibrium profiles of η and θ plotted along x_1 direction. Results with increasing number of finite elements are shown together with the analytic solution. Zoomed in views on the lower-right corners reveal the small differences.

point level. The communication between them is handled through the MGIS:fenics library (Helfer et al., 2020), which we modified and extended for our purposes. The details of the implementation including the weak forms, update of state variables and some numerical considerations are presented in Appendix C. The system of equations is solved with a monolithic approach, where -in two dimensions- each node has 4 degrees of freedom: order parameter η, Cosserat microrotation θ and 2 displacements (u_1, u_2). A semi-implicit time discretization is used and the resulting nonlinear system of equations is solved using the Newton–Raphson procedure (cf. Appendix C for details). Enforcing constraint (9) allows us to identify the lattice orientation with Cosserat microrotation $\boldsymbol{\Theta}$, which has only one non-zero component in two-dimensions, the in-plane rotation θ. It is measured with respect to the fixed global coordinate system given in Fig. 1. The constitutive equations are applied in the local material frame. A feature of the coupled model is that the continuous and evolving lattice orientation field θ is used to rotate between global and the material coordinate system.

3.1. Equilibrium profiles

Fig. 1 shows the two-dimensional periodic bicrystal structure used in most of the examples. There are two grains with 15° of misorientation, and the opposing surfaces along x_1 and x_2 directions are assumed periodic. Each grain has a width of 10 μm in x_1 direction, and a height of 2 μm in x_2 direction. However, due to periodic boundaries, the solution field is constant along x_2, so the length along x_2 is only for visualization purposes. The displacements are set to $\underline{\boldsymbol{u}} = \underline{\mathbf{0}}$ unless stated otherwise. In the absence of displacements, when the constraint $\overset{\times}{\underline{\boldsymbol{e}}}^{\mathrm{e}} \equiv 0$ is satisfied by using a sufficiently high Cosserat penalty parameter μ_c, the coupled model should reproduce the equilibrium profiles for η and θ at grain boundaries obtained from the asymptotic solution given in Appendix A for pure the HMP phase field. We validate this with the model parameters given in Table 1.

Second order triangular elements with reduced integration are used. Along x_1, we performed a mesh convergence study using 250, 500 and 1000 blocks consisting of two triangular finite elements. Since the solution is invariant in x_2 direction, only one block is used in this direction. The initialization of the solution variables is crucial to achieve initial convergence in the Newton–Raphson iterations. The orientation field θ is initialized by using a hyperbolic tangent in the form of (B.9) with $c = 20$. Using such a smooth function instead of a step function improves the convergence behavior. To ensure that the coupling function $g(\eta)$ is not singular initially [it becomes singular at $g(\eta = 1)$, cf. Eq. (48)], the order parameter η is initialized to a constant value of $\eta_0 = 0.99$. Finally, in the undeformed state, in order to make sure that there is no initial elastic strain, we need to set $\overset{\times}{e}{}^*(t = 0) = -\theta(t = 0)$ as shown in Eq. (39).

We let the fields evolve using time increment size $\Delta t = 0.1\,\mathrm{s}$ until $t = 10\,\mathrm{s}$, at which the system reaches equilibrium. The resulting profiles are shown in Fig. 2 for different levels of discretization. With 1000 blocks we obtained excellent agreement with the analytical solution. Even with 250 blocks, the difference is minimal to the naked eye. The grain boundary width is about 0.4 μm, which is in an acceptable range for diffuse grain boundary models.

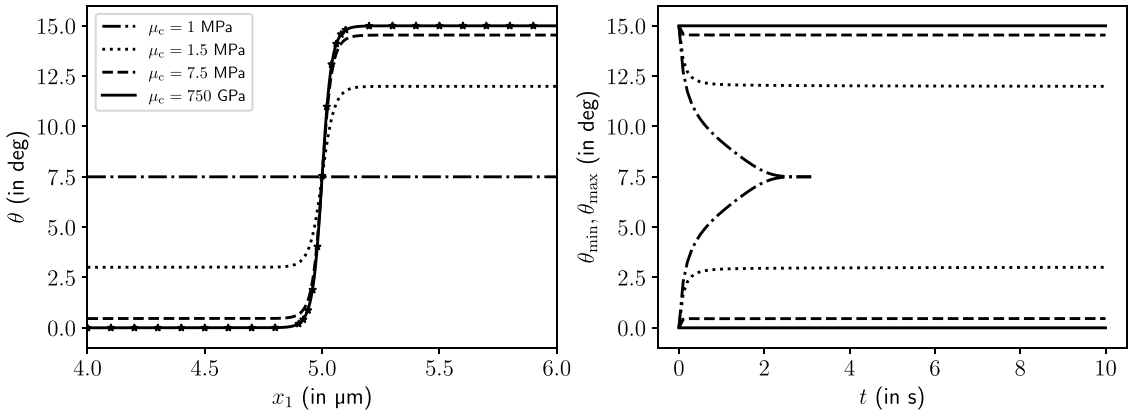

Fig. 3. Equilibrium profiles θ plotted at $t = 10$ s along x_1 direction for varying Cosserat penalty parameter μ_c (left), where stars represent $-\overset{\times}{e}{}^*$. Change of orientation in each grain with time (right).

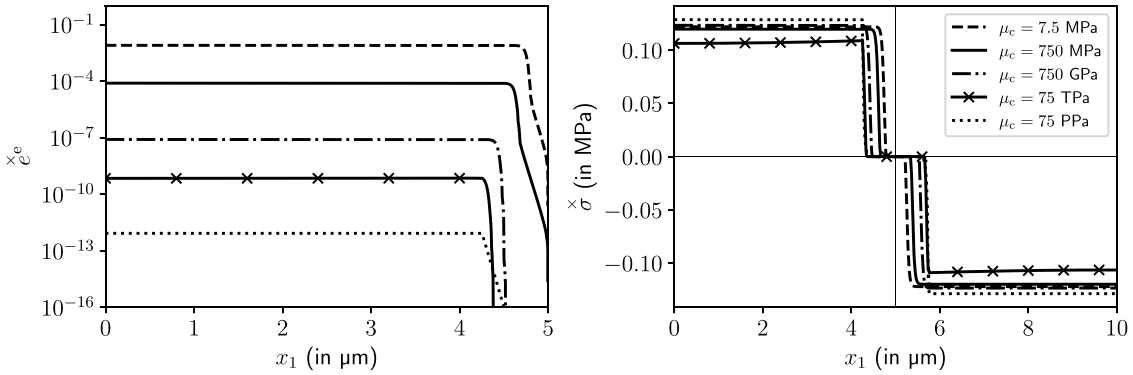

Fig. 4. Skew part of the elastic strain $\overset{\times}{e}{}^e$ (left) and stress $\overset{\times}{\sigma}$ plotted at $t = 100$ s along x_1 direction for varying Cosserat penalty parameter μ_c.

For the results in Fig. 2, we have used $\mu_c = 750$ GPa which was sufficiently high to satisfy the constraint $\underset{\sim}{\overset{\times}{e}}{}^e \equiv 0$. Next, we examine what happens if smaller or larger values of μ_c are used. Without displacement and slip, the only component of the skew part of stress is given by

$$\overset{\times}{\sigma} = 2\mu_c \overset{\times}{e}{}^e = 2\mu_c(-\overset{\times}{e}{}^* - \theta), \tag{56}$$

which is initialized to zero. When μ_c is high, in order to satisfy balance Eq. (13), $\overset{\times}{e}{}^e$ is forced to be small. If μ_c is smaller, we would expect that $\overset{\times}{e}{}^e$, thus the difference between $\overset{\times}{e}{}^*$ and θ grows. The evolution of $\overset{\times}{e}{}^*$ is governed by

$$g(\eta)\hat{\tau}_* \overset{\times}{e}{}^* = \overset{\times}{\sigma}, \tag{57}$$

which is hindered in the bulk of the grains due to the singular function $g(\eta)$. Therefore, in the case of smaller μ_c, θ should evolve away from $-\overset{\times}{e}{}^*$, meaning that in our bicrystal example the two grains should rotate towards each other to minimize energy. This hypothesis is confirmed in Fig. 3, where for $\mu_c = 1$ MPa the grains quickly rotate towards each other until they have the same orientation. Note that this is not the same θ relaxation mechanism observed in the pure HMP or KWC phase field models. The difference can be seen for cases $\mu_c = 1.5$ and 7.5 MPa, in which grains rotate a bit but then stop rotating, when they reach equilibrium at some misorientation. This rotation decreases as μ_c increases, and it is not noticeable for $\mu_c = 750$ GPa, where θ remains close to $-\overset{\times}{e}{}^*$.

Fig. 4 shows the difference between $-\overset{\times}{e}{}^*$ and θ, or, equivalently, the skew part of elastic strain $\overset{\times}{e}{}^e$, for larger μ_c. At $\mu_c = 750$ GPa, $\overset{\times}{e}{}^e$ is indeed negligible, and becomes smaller if μ_c is increased further. In fact, $\overset{\times}{e}{}^e$ appears to be inversely proportional to μ_c. Another observation is that the value of $\overset{\times}{e}{}^e$ is many orders of magnitude smaller inside the grain boundary as compared to the bulk, even effectively zero for $\mu_c > 750$ GPa. This is in agreement with Eq. (57), as $\overset{\times}{e}{}^*$ evolves a lot faster inside the grain boundary and is able to match $-\theta$. Fig. 4 also shows the skew part of stress $\overset{\times}{\sigma}$, which is the driving force for $\overset{\times}{e}{}^*$ evolution. Although μ_c changes significantly, the stress $\overset{\times}{\sigma} = 2\mu_c \overset{\times}{e}{}^e$ is relatively similar for all cases, since μ_c and $\overset{\times}{e}{}^e$ change proportionally. The non-zero stress inside the grains shows that even with very high μ_c, $\overset{\times}{e}{}^*$ will change in time and, as a result, the orientation field θ will change. However, thanks to $g(\eta)$ slowing down the $\overset{\times}{e}{}^*$ evolution, this rotation remains negligible, i.e., $\approx 10^{-10}$ (see Fig. 5), in the simulation time of 100 s.

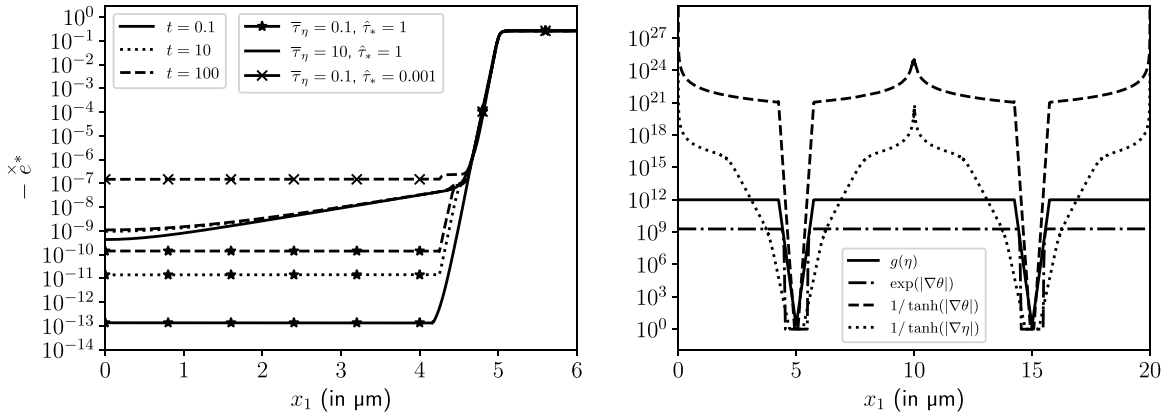

Fig. 5. Eigenrotation $\overset{\times}{e}^*$ at different times (left) and various localization functions at $t = 100$ s (right) plotted along x_1 direction. For the localizing functions (52) the following parameters are used $\overline{\mu}_\mathrm{p} = 10^9$, $\beta_\mathrm{p} = 10^2$, $\overline{\epsilon} = 0.5$ and $\overline{C}_* = \sqrt{10}$.

The evolution of $\overset{\times}{e}^*$ plays a central role for the equilibrium profile. It is also significant for the grain boundary migration dynamics, which is discussed in Section 3.4. Therefore, it is important understand how its evolution is localized to the grain boundaries in Eq. (57), and how the model parameters affect it. Fig. 5 shows the change of $\overset{\times}{e}^*$ in time with $\mu_\mathrm{c} = 750\,\mathrm{GPa}$ for two different inverse mobility parameters $\overline{\tau}_\eta$: 0.1 and 10. At $t = 0$, $\overset{\times}{e}^*$ is initialized to zero in the outer grain. For $t = 0.1$ the value of $\overset{\times}{e}^*$ is different by several orders of magnitude for the two cases. As time passes, the eigenrotation keeps increasing in both cases, which is caused by the skew-symmetric stress shown in Fig. 4. Further, for $\overline{\tau}_\eta = 10$, unlike $\overline{\tau}_\eta = 0.1$, the eigenrotation is not constant inside the bulk. This difference is due to our localizing singular function $g(\eta)$ in (57). When $\overline{\tau}_\eta$ is increased, η evolves slower, from its initial value of 0.99, meaning $g(\eta)$ is not as large as $g(1)$ initially. Thus, when η evolves slowly towards 1, $g(\eta)$ fails to prevent the $\overset{\times}{e}^*$ evolution inside the grains. Therefore, $\overline{\tau}_\eta$ should be chosen sufficiently small such as $\overline{\tau}_\eta = 0.1$. Another option is to initialize η closer to 1, i.e. 0.9999, which however makes the initial convergence harder. Looking at Eq. (57), the effect of $\hat{\tau}_*$ on $\overset{\times}{e}^*$ is clear: the rate of $\overset{\times}{e}^*$ is inversely proportional to $\hat{\tau}_*$. This is observed in Fig. 5 when $\hat{\tau}_* = 0.001$ is used instead of $\hat{\tau}_* = 1$. Consequently, using a larger $\hat{\tau}_*$ seems beneficial for obtaining the equilibrium profile, however this has a negative effect on grain boundary mobility as discussed in Section 3.4.

Another important factor for $\overset{\times}{e}^*$ evolution is the function that localizes it to grain boundaries. As mentioned in the previous section, the KWC-CCP coupled model is presented with different localizing functions, shown in (52), throughout the development (Ask et al., 2018a, 2019, 2020). In our model, we use the singular coupling function $g(\eta)$, which is the cornerstone of the HMP phase field model (Henry et al., 2012; Staublin et al., 2022), instead. These different localizing functions are plotted and compared in Fig. 5. Note that the $g(\eta)$ shown actually has a finite value of 10^{12} inside the grains. This is because we use a predefined cut-off value of 0.9999 to calculate g and g' during numerical simulations (see Appendix C), which improves numerical stability and the convergence behavior of the model significantly. Similarly, Ask et al. (2020) have used a smoother and less strict exponential form compared to previous hyperbolic tangent forms in Ask et al. (2018a, 2019). The $\tanh(|\nabla\eta|)$ form has a wider distribution around the grain boundary, which is not ideal for localization. The $\tanh(|\nabla\theta|)$ form has a similar distribution compared to $g(\eta)$, but takes very large values inside the grains. In our simulations we have observed that tanh forms result in peaks of $\overset{\times}{e}^e$ near grain boundaries, while the function $g(\eta)$ provides a good balance between smoothness and localization; moreover, we can control its value inside the grains using the cut-off value.

3.2. Triple-junction test

In this section we perform the so called triple-junction test with the geometry shown in Fig. 6. The three grains have different orientations with the corresponding misorientations at the grain boundaries given by $\Delta\theta_1$, $\Delta\theta_2$ and $\Delta\theta_3$. The orientations are held constant by applying Dirichlet boundary conditions on η and θ. Under these conditions, the triple junction moves to an equilibrium point and stops. The angles of the intersection at the equilibrium are given by Herring's force balance (Herring, 1951), which simplifies to Young's Law for isotropic grain boundaries

$$\frac{\gamma_1}{\sin(\alpha_1)} = \frac{\gamma_2}{\sin(\alpha_2)} = \frac{\gamma_3}{\sin(\alpha_3)}, \tag{58}$$

where γ_i are grain boundary energies and α_i are dihedral angles. We test the proposed coupled model by using different misorientations with parameters in Table 1, to see if correct dihedral angles according to (58) are obtained. While this test has been already performed in previous work (Henry et al., 2012; Staublin et al., 2022) for the original HMP orientation phase field, we use a different potential $V(\eta)$ and the orientation evolution is governed by Cosserat mechanics.

The geometry is divided into 100 × 100 blocks where each block contains four second order triangular finite elements with reduced integration. The simulations are continued until time-independent solutions are obtained. The triple junction angles from

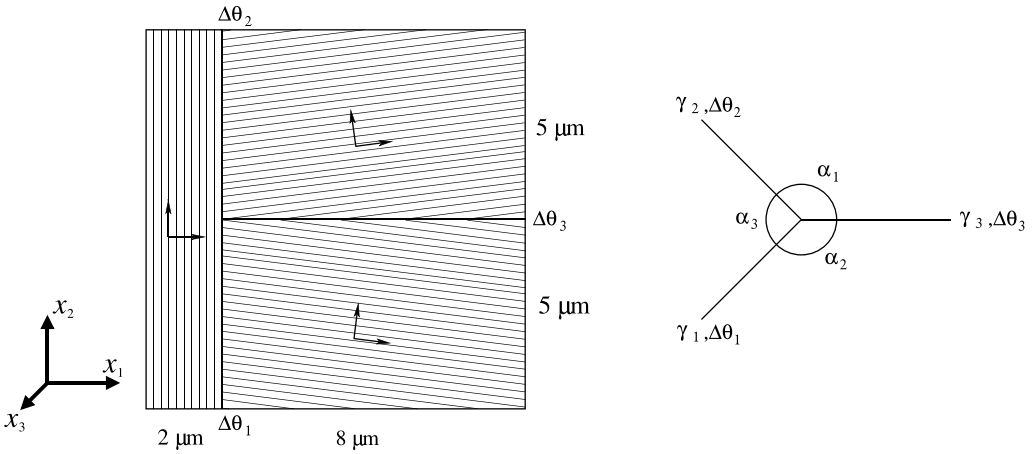

Fig. 6. Triple junction test geometry and the dihedral angles at the junction.

Table 2
Equilibrium triple-junction angles obtained from finite element simulations and Herring's equation.

Misorientation			GB energy (in J/m^2)			FE angles (Herring)		
$\Delta\theta_1$	$\Delta\theta_2$	$\Delta\theta_3$	γ_1	γ_2	γ_3	α_1	α_2	α_3
5°	5°	10°	0.2435	0.2435	0.3914	143.6° (143.5°)	143.6° (143.5°)	72.8° (73.0°)
7.5°	7.5°	15°	0.3235	0.3235	0.5018	141.0° (140.9°)	141.0° (140.9°)	78.0° (78.2°)
10°	10°	20°	0.3914	0.3914	0.5883	138.8° (138.7°)	138.8° (138.7°)	82.4° (82.6°)
20°	20°	40°	0.5883	0.5883	0.8038	132.2° (133.1°)	132.2° (133.1°)	95.6° (93.8°)
30°	30°	60°	0.7154	0.7154	0.9146	130.1° (129.7°)	130.1° (129.7°)	99.8° (100.6°)
20°	15°	5°	0.5883	0.5018	0.2435	80.4° (81.8°)	122.7° (122.4°)	156.9° (155.8°)
10°	5°	15°	0.3914	0.2435	0.5018	130.6° (130.3°)	151.6° (151.7°)	77.8° (78.0°)

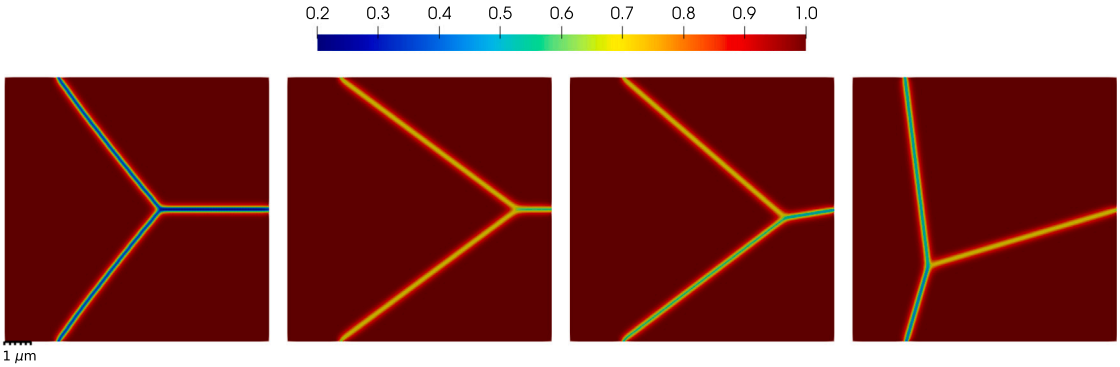

Fig. 7. Order parameter contours at equilibrium for the triple junction problem with different misorientations $\Delta\theta_1/\Delta\theta_2/\Delta\theta_3$. From left to right: 30°/30°/60°, 5°/5°/10°, 10°/5°/15° and 20°/15°/5°.

Young's Law (58) and the angles from finite element results are compared in Table 2. The grain boundary energies used in (58) are found from 1D grain boundary simulations for the given discretization. The angles are measured along the lines of minimum η, i.e., the center of the grain boundary.

As seen in Table 2, the agreement is very good. Fig. 7 shows the η fields after equilibrium is reached, where the equilibrium positions are clearly different. Note that the GB energies at misorientations higher than 30° in Table 2 are not physically realistic, since we are assuming a simple monotonically increasing curve in Fig. A.19. However, this has no effect for our purpose of comparing the numerical dihedral angles with the analytical solution in Eq. (58). With these we confirm that the mechanics coupled phase field model is working as intended.

3.3. Elastic shear loading

In this section we test the behavior of the model under mechanical loading. The same periodic bicrystal structure as in Section 3.1 is used with 1000 blocks of second order triangular elements with reduced integration along x_1 direction. The loading is applied by

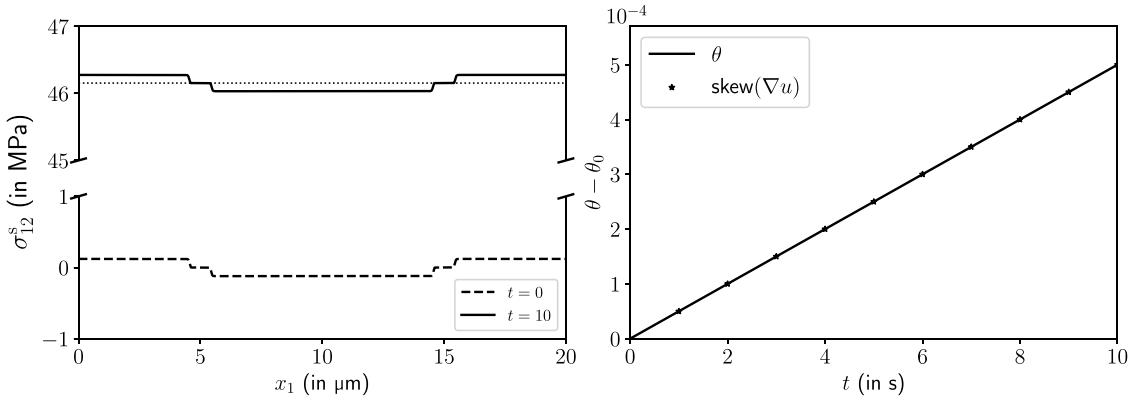

Fig. 8. Stress profile before and after simple shear loading for isotropic elasticity, where the dotted line shows analytic solution (left). Cosserat rotation and lattice rotation (right).

imposing a mean displacement field with periodic fluctuations as explained in Appendix B. The total displacement $\underline{\boldsymbol{u}}$ is given by,

$$\underline{\boldsymbol{u}} = \underset{\sim}{\boldsymbol{B}} \cdot \underline{\boldsymbol{x}} + \underline{\boldsymbol{v}} \tag{59}$$

where the tensor $\underset{\sim}{\boldsymbol{B}}$ is defined as,

$$\underset{\sim}{\boldsymbol{B}} = \begin{bmatrix} 0 & B_{12} & 0 \\ B_{21} & 0 & 0 \\ 0 & 0 & 0 \end{bmatrix} \tag{60}$$

for shear loading with $B_{21} = 0.001$ and $B_{12} = 0$. The periodic fluctuation $\underline{\boldsymbol{v}}$ is fixed at the corners. The loading is applied until $t = 10\,\mathrm{s}$ with $\Delta t = 0.1\,\mathrm{s}$. In order to compare our numerical results we assume that the material is elastic, since it is possible to find analytic solution for this problem. We consider two test cases, namely isotropic and cubic elasticity.

3.3.1. Isotropic elasticity

For the case of isotropic elasticity, the model parameters given in Table 1 are used except for the elastic constants, for which we assume Young's modulus $E = 120\,\mathrm{GPa}$ and Poisson's ratio as $\nu = 0.3$. Before applying the loading, we first initialize the order parameter and orientation field similar to Section 3.1 and evolve these fields until reaching an equilibrium. However, unlike the first example, the displacement degree of freedom is not restricted, i.e. $\underline{\boldsymbol{u}} \not\equiv 0$. The obtained fields η, θ, $\overset{\times}{\underset{\sim}{\boldsymbol{e}}}{}^{*}$ and $\underline{\boldsymbol{u}}$ are used as initial conditions in the loading stage. When $\underline{\boldsymbol{u}}$ is not fixed, we have an initial symmetric stress distribution at $t = 0$ as seen in Fig. 8, where $\underset{\sim}{\boldsymbol{\sigma}}^{s} = \underset{\approx}{\boldsymbol{E}}^{\mathrm{s}} : \underset{\sim}{\boldsymbol{\varepsilon}}^{\mathrm{e}}$, in addition to the skew-symmetric stress $\overset{\times}{\underset{\sim}{\boldsymbol{\sigma}}}$. This initial symmetric stress will be referred to as a residual stress from here on. The reason for this residual stress is the tendency of the grains to rotate towards each other. In the HMP or KWC orientation phase field models, one of the evolution mechanisms to minimize free energy is to reduce misorientation by the rotation of grains. This rotation can be suppressed by using a varying mobility function such as (52) or (53). In the coupled model, the magnitude of the driving force for this rotation is given by $\overset{\times}{\underset{\sim}{\boldsymbol{\sigma}}}$ as shown in Fig. 4. Hence, when displacements are free in Fig. 1, the outer grain rotates counter-clockwise and the inner grain rotates clockwise. Thus, in order to satisfy continuity at the grain boundaries, both grains must be strained, which we observe as the residual stress in Fig. 8. The residual stress is zero in the vicinity of grain boundaries, since it is relaxed quickly according to (38) by the evolution of $\overset{\times}{\underset{\sim}{\boldsymbol{e}}}{}^{*}$. Since the magnitude of residual stress is related to the driving force for grain rotation, it is smaller for higher misorientations, and for grain boundaries that are further away. In our example it is quite small, approximately 0.125 MPa, and it is magnified in Fig. 8 for clarity.

For the isotropic case, the stress distribution after loading should be the same in both grains, since there is no orientation dependence. The analytic solution is straightforward and given by the only non-zero component $\sigma^s_{12} = 46.15\,\mathrm{MPa}$, which is shown as dotted line in Fig. 8. The final stress from the simulation is the same as analytic solution if residual stress is excluded. On the right of Fig. 8, the change of lattice rotation skew(∇u) and Cosserat rotation θ are shown as functions of time. They are equal as desired and change linearly as expected. The coupled model allows the continuous orientation field θ to evolve due to mechanical loading.

3.3.2. Cubic elasticity

In the case of cubic anisotropy, elastic constants are taken as $C_{11} = 160\,\mathrm{GPa}$, $C_{12} = 110\,\mathrm{GPa}$ and $C_{44} = 75\,\mathrm{GPa}$. Due to anisotropy and the different orientations of the grains, the final stress field includes components other than shear, as shown in Fig. 9. For the given boundary conditions, it is possible to find an analytic solution as explained in Appendix B. The analytic results are plotted with markers on top of the numerical solution in Fig. 9, showing excellent agreement. Note that, similar to the isotropic case, we have small residual stresses after initializing the order parameter and orientation field. Fig. 9 (right) again shows the lattice and Cosserat rotations together, but this time they are different at each grain due to anisotropy. As expected, for high Cosserat penalty parameter (μ_c) values, the Cosserat rotation θ represents the lattice rotation $\left[\mathrm{skew}(\nabla u)\right]$.

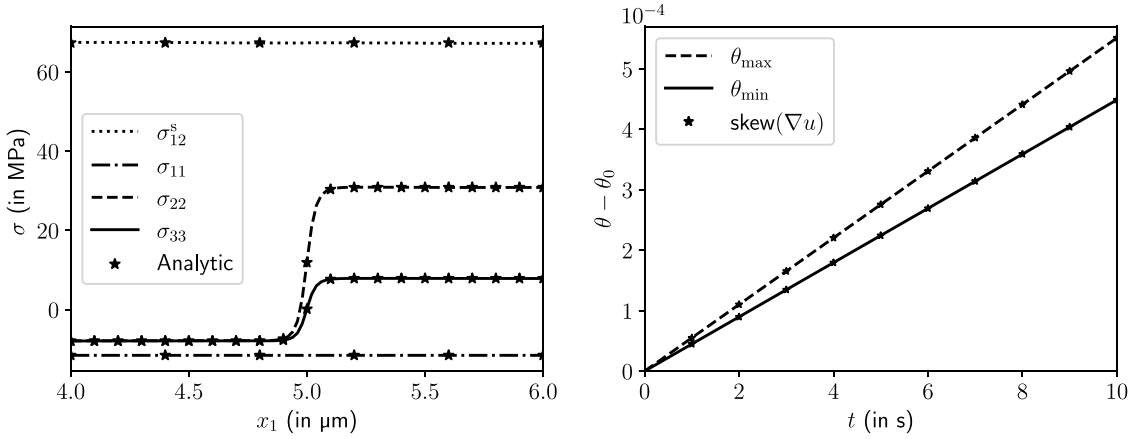

Fig. 9. Stress profiles at $t = 10$ after simple shear loading for cubic anisotropy, where stars show the analytic solution (left). Cosserat rotation and lattice rotation for grains with 0° ($\theta_{\min}$) and 15° ($\theta_{\max}$) orientation (right).

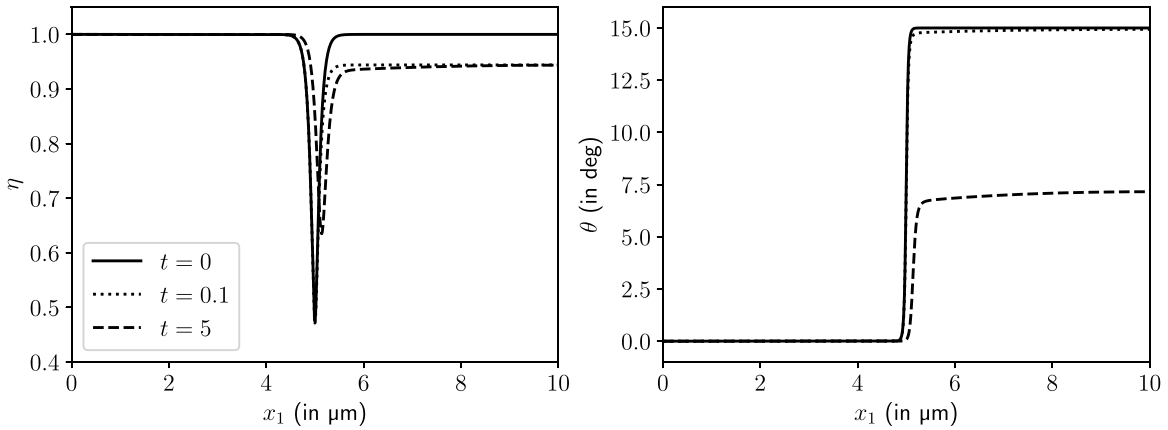

Fig. 10. Profiles of η and θ at different times when SSD energy multiplier function is $\phi(\eta) = \eta$, and inner grain has stored SSD density of $\rho = 10^{15}$ m^{-2}.

3.4. Grain boundary migration due to stored dislocations

In this section the mechanism of grain boundary migration driven by statistically stored dislocations is discussed. During plastic deformation of a polycrystal, SSDs are most likely generated non-uniformly, which causes stored energy gradients. In the free energy (22), assuming single slip system for simplicity, stored energy of dislocations is given by the term $\phi(\eta)\frac{\lambda}{2}\mu^{\mathrm{e}}b^2\rho$, which can cause an energy gradient depending on the distribution of $\rho(\underline{x})$. Moreover, for the evolution of the phase field, due to the term $\phi(\eta)$, this results in the driving force $f_\eta = \phi_{,\eta}(\eta)\frac{\lambda}{2}\mu^{\mathrm{e}}b^2\rho$. We test this mechanism using the same periodic bicrystal example in Fig. 1. The SSD density ρ_0 is initialized as 10^{15} m^{-2} in the inner grain, resembling cold worked copper (Rollett et al., 2017) and as zero in the outer grain. The shear modulus μ^{e} is given by $C_{44} = 75$ GPa for cubic elasticity, the Burgers vector for pure copper is $b = 0.2556$ nm and $\lambda = 0.3$. The mobility constant for $\overset{\times}{\underline{e}}{}^*$ is taken as $\overline{\tau}_* = 0.01$ and, to counter the increased mobility, the cut-off of $g(\eta)$ taken as $(1 - 10^{-5})$. The rest of the parameters are given in Table 1. The same mesh as in previous example is used , but displacements $\underline{u}$ are set to zero. The solution fields are initialized with the equilibrium values from Section 3.1.

We first used $\phi(\eta) = \eta$ following Abrivard et al. (2012) and Ask et al. (2018a), which does not work for the HMP phase field coupled model as seen in Fig. 10. While the grain boundary moves towards the grain with stored SSDs, the initial orientation of the inner grain is not preserved. This is a consequence of the way Abrivard et al. (2012) formulated $\phi(\eta)$; from Eq. (55) the order parameter η stabilizes at a value $\eta < 1$ given by

$$\eta^{\mathrm{eq}} = 1 - \frac{\phi_{,\eta}\frac{\lambda}{2}\mu^{\mathrm{e}}b^2\rho}{f_0\alpha} \quad \text{with} \quad \phi_{,\eta} = 1, \tag{61}$$

which results in $\eta^{\mathrm{eq}} \approx 0.944$ for the given parameters, as seen in Fig. 10. This is incompatible with the HMP model, since it relies on the singular function $g(\eta)$ to localize and distinguish between grain boundaries and bulk of grains, and η must be close to 1 for

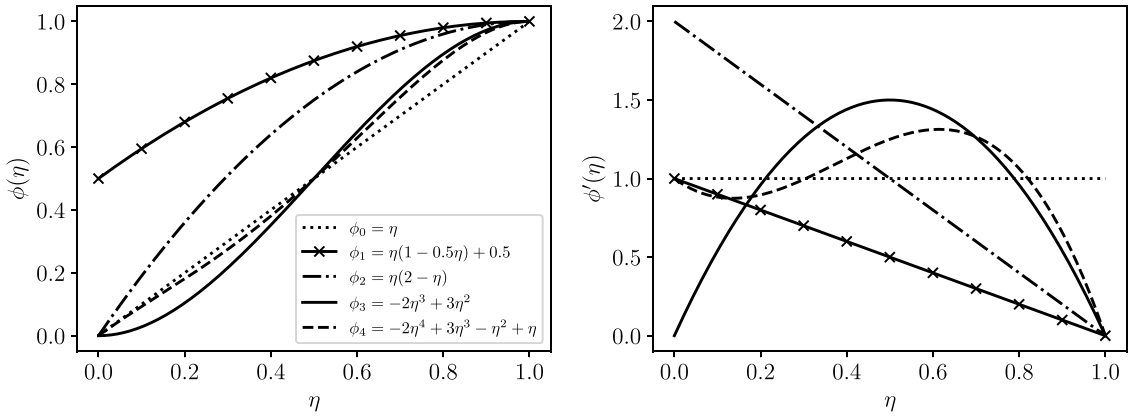

Fig. 11. Different possible forms of the multiplier function $\phi(\eta)$ for the SSD energy and their derivatives $\phi'(\eta)$.

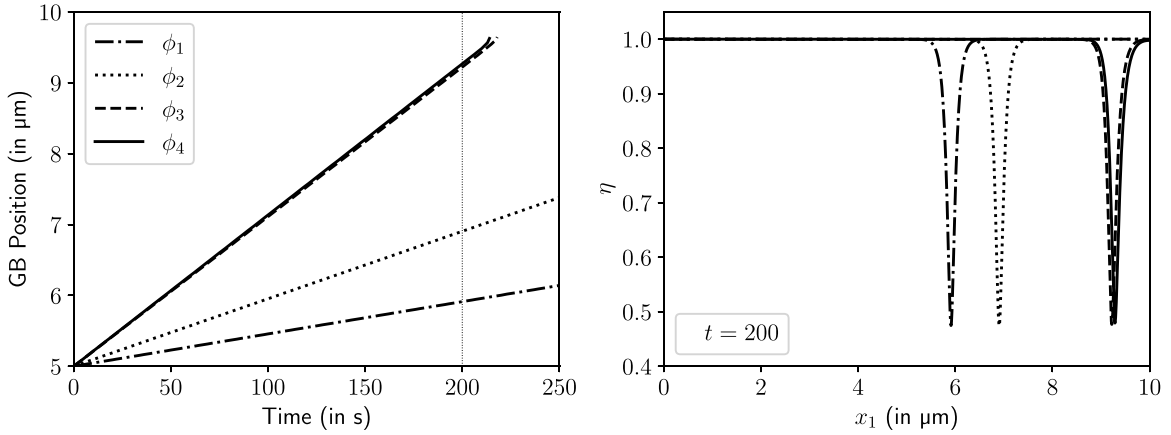

Fig. 12. Grain boundary position in time for different forms of the multiplier function $\phi(\eta)$ for the SSD energy (left), and order parameter η profile for each at $t = 200$ s (right).

$g(\eta)$ to be singular. Therefore, we propose a modified $\phi(\eta)$, which preserves $\eta^{\text{eq}} = 1$ even if SSDs are present. Looking at (61), this is possible if

$$\phi_{,\eta}(1) = 0 \quad \text{and} \quad \phi(\eta) > 0 \quad \text{for} \quad 0 < \eta < 1, \tag{62}$$

where the second condition ensures the positivity of energy although it is not mandatory. Several polynomial forms satisfying these conditions are shown in Fig. 11 along with their derivatives, representing the driving force on the order parameter.

Fig. 12 shows the motion of the grain boundary for each of the polynomials in Fig. 11. The left figure shows the position of the grain boundary in time; clearly, the velocity differs depending on the form of $\phi(\eta)$ with ϕ_3 and ϕ_4 being very similar. The right figure shows the η profiles at $t = 200$ s, where we can see that the $\eta^{\text{eq}} = 1$ condition is satisfied for all $\phi(\eta)$. The forms of ϕ_3 and ϕ_4 are chosen to be as similar as possible to $\phi_0 = \eta$. In our tests, comparing the different forms of ϕ using the KWC-Cosserat coupled model, we have observed that ϕ_3 and ϕ_4 provide velocities comparable to $\phi_0 = \eta$, while ϕ_1 and ϕ_2 significantly reduce velocity. The velocity appears to be proportional to the value of $\phi'(\eta)$ at $\eta > 0.5$ shown in Fig. 11 (right). This observation is consistent with the fact that the grain boundary is represented with order parameter values $0.5 < \eta < 1$ for the given misorientation as seen in Fig. 2. Therefore, in the remaining examples we use the 4th order polynomial form $\phi_4(\eta)$, which is most similar to $\phi_0 = \eta$.

Fig. 13 shows the profiles of η, θ, $\underset{\sim}{\overset{\times}{e}}^*$, ρ and $\overset{\times}{\sigma}$ at different times. At $t = 0$, the inner grain is initialized with $\rho_0 = 10^{15}$, as seen in Fig. 13(c), while η, θ and $\overset{\times}{\sigma}$ have the respective equilibrium profiles. $\overset{\times}{\sigma}$ is non-zero inside the grains, as discussed in Section 3.1, showing the tendency to rotate, but is held in place by a high Cosserat penalty parameter μ_c. As the simulation is run, the energy gradient due to the inhomogeneous SSD distribution drives the grain boundaries to move towards the grain with the higher energy. In the wake of the moving grain boundary, static recovery can take place, which is a phenomenon observed in experiments (Bailey and Hirsch, 1962). In the model this is implemented with Eq. (41) following Abrivard et al. (2012). If the recovery parameter C_D in (41) is sufficiently large, i.e. 100, full recovery occurs and ρ reduces to zero in the wake of the sweeping boundary, as seen in Fig. 13(c). While this is not realistic in general, the amount of remaining defects can be adjusted by changing C_D, as shown later in Section 3.5.

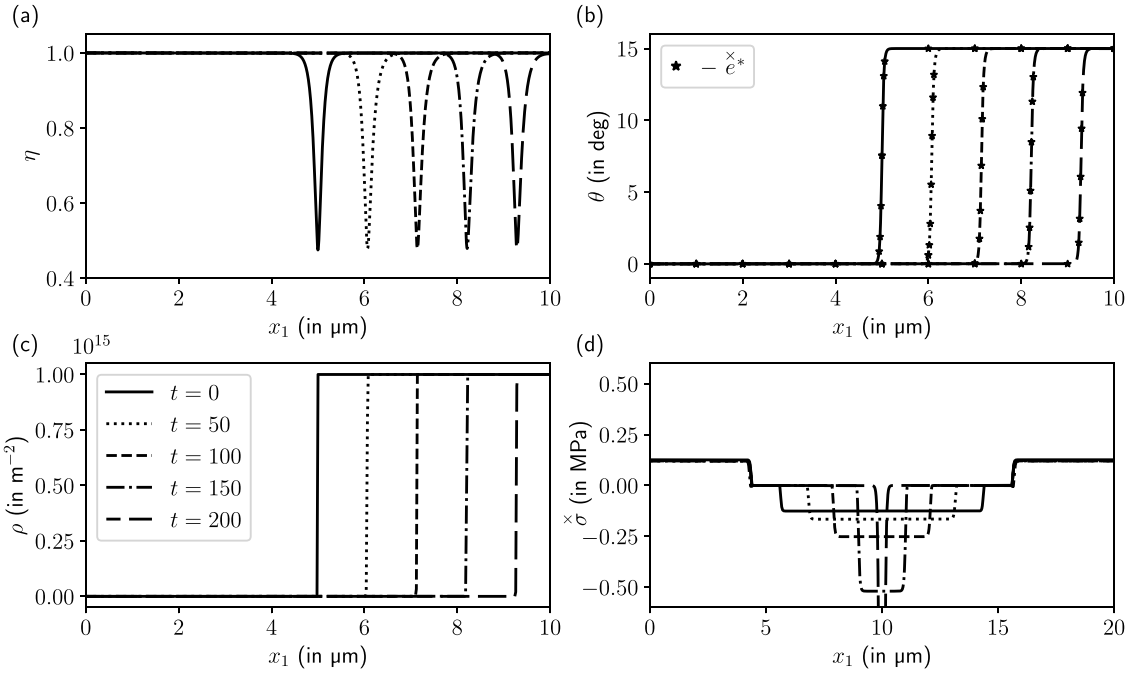

Fig. 13. Grain boundary migration snapshots at different times, where the SSD energy multiplier ϕ_4 is used with $\overline{\tau}_* = 0.01$. Profiles of phase field η (a), orientation θ and $-\overset{\times}{e}^*$ as stars (b), SSD density ρ (c) and skew-stress $\overset{\times}{\sigma}$ (d) are shown.

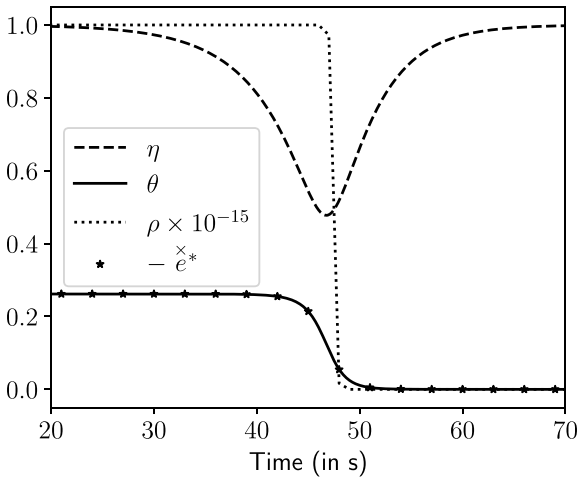

Fig. 14. Evolution of solution variables in time on a point located at $x = 6\,\mu\text{m}$ in Fig. 13.

In Fig. 13(b) we see that the orientation field θ evolves with the moving grain boundary, and the reference orientation $\overset{\times}{\underline{e}}^*$ follows the movement according to Eq. (57), ensuring that the strain free state is maintained. Moreover, the evolution of $\overset{\times}{\underline{e}}^*$ inside the sweeping grain boundary fully relaxes the initial skew stress $\overset{\times}{\sigma}$ in the wake as seen in Fig. 13(d). Also, we see an increase of $\overset{\times}{\sigma}$ in the inner grain as the grain boundaries move closer, which shows that there is a stronger tendency to rotate as grain size decreases. Fig. 14 shows the evolution of main fields in time at the fixed location $x_1 = 6\,\mu\text{m}$. The SSD density smoothly reduces to zero as discussed by Abrivard et al. (2012), while θ and $\overset{\times}{\underline{e}}^*$ evolve together.

The co-evolution of θ and $\overset{\times}{\underline{e}}^*$ is crucial, and it may not be maintained depending on the value of the inverse mobility τ_*. Fig. 15 (left) shows the grain boundary position in time for different $\overline{\tau}_*$. It seems that above a certain threshold, the motion is disturbed and the grain boundary velocity decreases. When $\overline{\tau}_*$ is small enough, the velocity is not affected. As also observed by Ask et al. (2018a), a good rule of thumb is to set the mobility $\overline{\tau}_*$ smaller than phase field mobility; hence, we have used $\overline{\tau}_* = 0.01$ and $\tau_\eta = 0.1$ in this section. Fig. 15 (right) shows $\overset{\times}{\sigma}$ at $t = 150\,\text{s}$ for different $\overline{\tau}_*$. When $\overline{\tau}_*$ is too large, the evolution of $\overset{\times}{\underline{e}}^*$ lags behind θ, and the skew stress is not fully relaxed in the wake of the grain boundary. In addition, the final coalescence and the annihilation of the inner

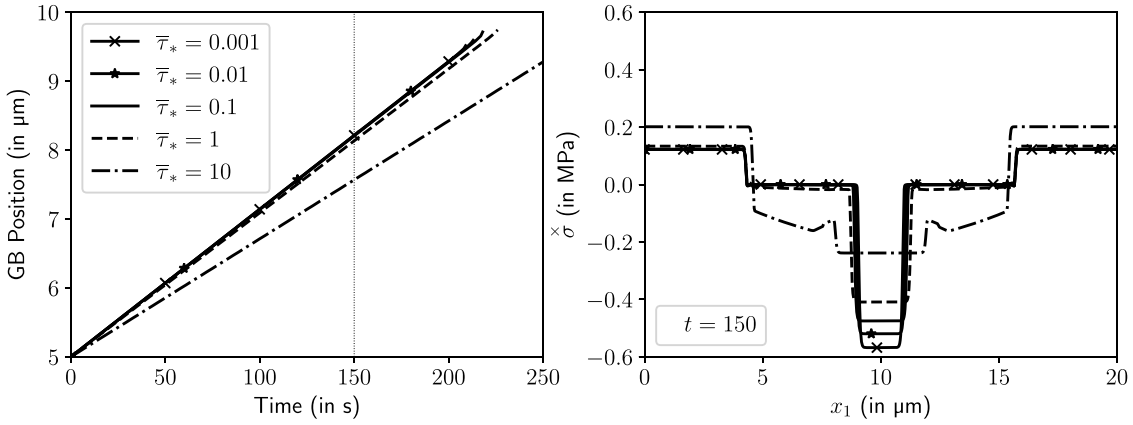

Fig. 15. Grain boundary position in time for different $\overline{\tau}_*$ (left), and skew-stress $\overset{\times}{\sigma}$ profile for each at $t = 150$ s (right).

grain happens slightly earlier for smaller $\overline{\tau}_*$, as evidenced by small peaks in Fig. 15 (left) towards the end, and higher values of $\overset{\times}{\sigma}$ in Fig. 15 (right).

3.5. Mechanical loading and migration

In this section the capability of the coupled HMP-Cosserat crystal plasticity model is explored based on a simple example, where the specimen undergoes plastic deformation and a subsequent SSD driven grain boundary migration at elevated temperatures. As shown in Ask et al. (2019), it is possible to illustrate this with the periodic bicrystal in Fig. 1 by applying a mean shear strain and then holding the mean deformation to simulate a heat treatment phase. The lattice orientations, dimensions, the finite element discretization and the boundary conditions are the same as the previous example. The material parameters given in Table 1 are used, except $\mu_c = 75\,\text{GPa}$ and $C_D = 25$. The former is reduced to improve the convergence, while keeping it sufficiently high to satisfy the constraint (9). Following the considerations from the previous section, inverse mobilities are set to $\overline{\tau}_* = 0.01$ and $\tau_\eta = 0.1$. We assume that a single slip system defined by

$$\underline{l}^1 = (1, 0), \qquad \underline{n}^1 = (0, 1), \tag{63}$$

is active. The dislocation density ρ is initialized to 10^{11} m^{-2} uniformly. Similar to Section 3.3 a mean shear is applied with a final value $B_{12} = 0.05$ and $B_{21} = 0$, which is ramped up linearly within 5 s. During loading, the recovery parameter C_D is set to zero. During the heat treatment phase the structure is evolved for 2000 s, during which $C_D = 25$. Unlike the example in the previous section, fluctuations $\underline{v}$ are free to evolve during the heat treatment phase.

In Fig. 16, the results of the proposed model are compared with the KWC-CCP model. While both HMP and KWC are orientation phase field models, their GB energetics are different since HMP does not have the $|\nabla\theta|$ term as opposed to KWC free energy [see Eqs. (22) and (49)]. To have a meaningful comparison, KWC parameters are calibrated to similarly have 0.5 J/m^2 GB energy at 15°, and fitted for misorientations less than 15° as shown in Fig. A.19, with the best fit in the range $10^\circ \div 15^\circ$, which matches the misorientations in our example. In Fig. 16(a) and (b), the difference at $t = 0$ in the initial profiles of η and θ can be seen, respectively, for the HMP-CCP and KWC-CCP models, where the latter has a slightly sharper profile. After loading at $t = 5$ s, the 0° orientated grains carry most of the plastic deformation due to the favorable alignment of the slip direction with the loading, resulting in a higher SSD density. The grains rotate towards each other due to deformation, decreasing the misorientation by about 5°, which can also be confirmed by the gradient of v_2 in Fig. 17. Since misorientation decreases [see Fig. 16(b)], the minimum value of η at the GB increases [see Fig. 16(a)], adapting to the changes in the microstructure. There is no noticeable difference in the deformation behavior of the two models, where the results are qualitatively similar to the findings of Ask et al. (2019). During the heat treatment phase, since there is a difference in the stored energy gradient, the grain boundary moves to reduce the energy, accompanied by the recovery of SSD and the change in the lattice orientation. GB velocities are clearly different, where the HMP-CCP velocity is faster for the same inverse mobility constant. For a given stored SSD energy gradient, the GB velocity is constant as shown in Fig. 15, and the inverse mobility τ_η can be adjusted to fit the velocities. The SSD density is recovered at the wake similar to previous examples, but here it reduces to a value on the order of 10^{12} instead of zero, which can be controlled by adjusting C_D. In Fig. 16(a) and (b) for the KWC model, the profiles of η and θ continue to change at the beginning of the heat treatment phase, indicating that the phase field did not have sufficient time to relax during the 5 s loading; this is not observed for the HMP model. This only shows that the HMP model evolves faster for the same mobility constant τ_η, and this behavior can be changed by adjusting τ_η for both models. Fig. 16 (d) shows the evolution of the critical resolved shear stress at both grains, which almost reaches saturation in the 0° grain. Fig. 17 shows the orientation evolution for the HMP-CCP model on the deformed specimen. It can be seen that, because of the strong coupling, the change in θ also evolves the displacement as the GB migrates. However, the periodicity of v_2 at the domain boundaries (see Fig. 17) imposes a very strong over-constraint, such that, when it is combined with the changes of v_2 at the GBs,

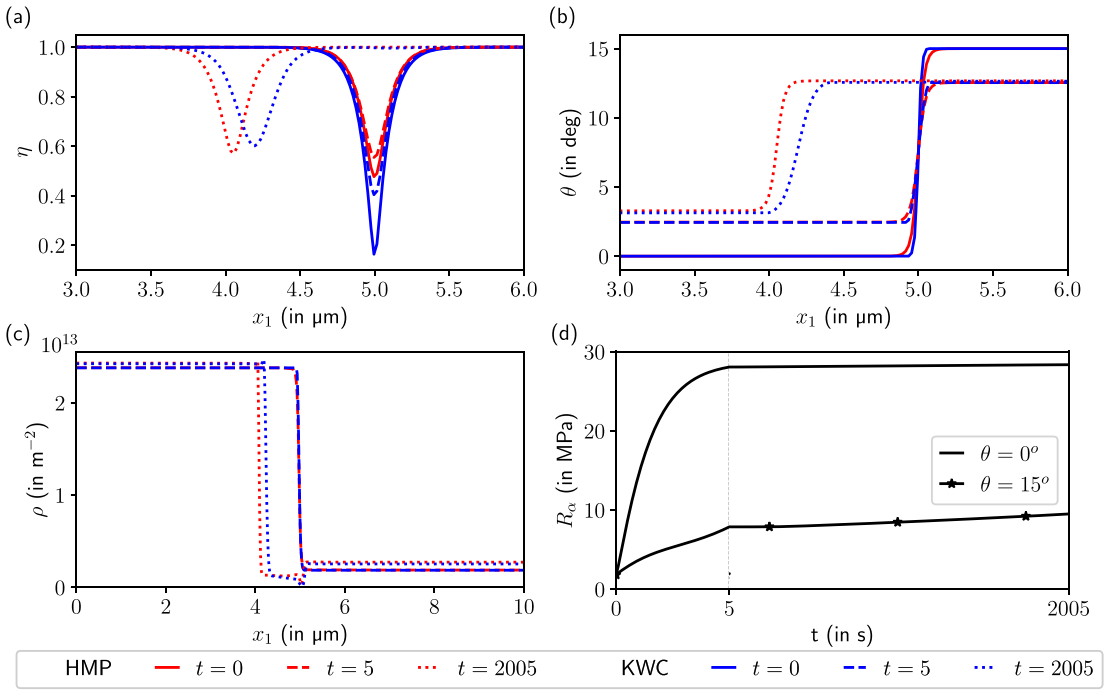

Fig. 16. Plastic deformation and subsequent grain boundary migration for the periodic bicrystal in Fig. 1. The sample is loaded in shear for 5 s, then heat treated until $t = 2005$ s using the HMP-CCP model and the KWC-CCP model as a reference. Order parameter η (a), orientation θ (b), SSD density ρ (c) and slip resistance R_α (for HMP-CCP) (d) are shown. The evolution of the slip resistance in (d) coincides for both models.

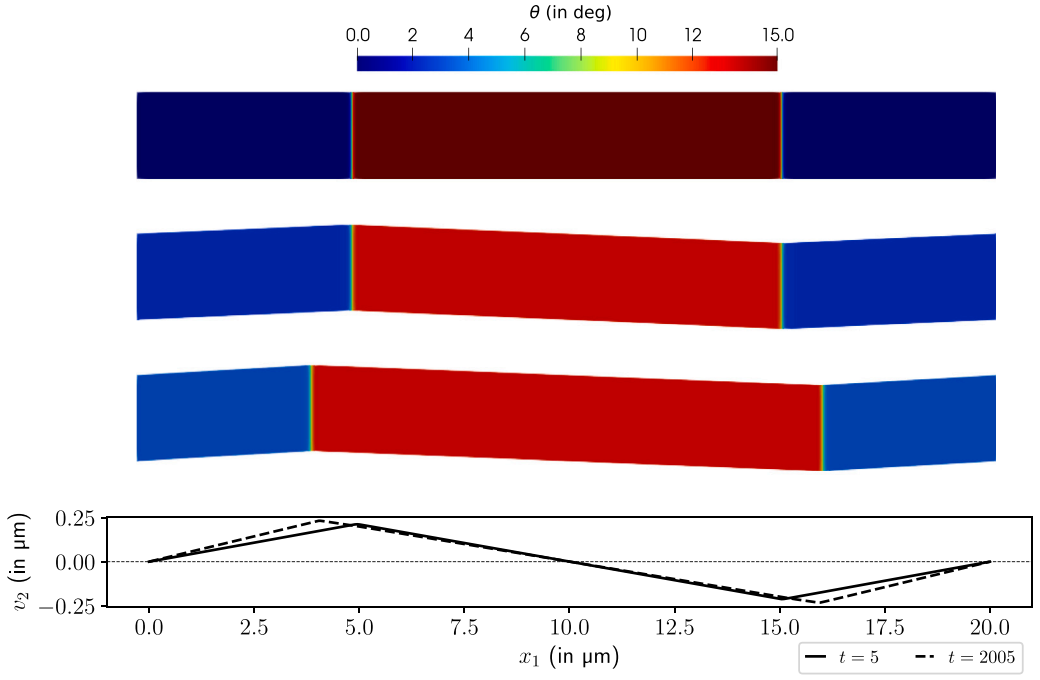

Fig. 17. Orientation contour evolution on the deformed specimen. From top to bottom: initial condition, after loading and after heat treatment. The line plot shows the evolution of fluctuation v_2.

the grains have to be sheared further to satisfy continuity. This non-intuitive deformation causes further generation of SSD, and bulk rotation as seen in Fig. 16 at $t = 2005\,\mathrm{s}$, which is a result of the simplified loading conditions.

4. Conclusion

We have presented a new multi-physics model coupling HMP type orientation phase field with the Cosserat crystal plasticity framework for evolution of grain boundary microstructure. The formulation of the model is inspired by the work of Ask et al. (2018a), which couples Cosserat mechanics to the KWC orientation phase field. The proposed model offers several improvements.

The main feature of the proposed model is the ability of the lattice orientation to evolve concurrently with both grain boundary migration and mechanical deformation. Firstly, the curvature driven grain boundary evolution mechanism is inherited from the HMP orientation phase field model, which was validated with a triple-junction test. Secondly, the lattice orientation is represented by the Cosserat micro-rotation through a constraint on the constitutive level. This makes its evolution by mechanical deformation consistent, which is tested with the elastic deformation of a periodic bicrystal. Similar to the KWC based coupled model, an eigen-deformation measure is introduced so that the stresses in the undeformed state are zero.

Another driving force for grain boundary migration is the non-homogeneous distribution of SSDs, which was incorporated into KWC with an SSD energy term (Abrivard et al., 2012). However, this enhancement alters the equilibrium state of the order parameter in an, at least in the HMP context, undesired way. We propose a modified form that preserves the same mechanism without altering the phase field equilibrium.

The capabilities of the strongly coupled framework were illustrated using the example of a periodic bicrystal, which is heat treated subsequent to plastic deformation. The deformation resulted in non-uniform changes in the lattice orientation of the grains and, similarly, non-uniform SSD generation. The SSDs create a driving force for the migration of GBs during heat treatment, leading to a partial or full recovery of dislocation density in the wake of the moving boundary.

By construction, the HMP model removes non-physical long range interactions between the grain boundaries that exist in the KWC model due to the $|\nabla\theta|$ term in the free energy. Moreover, the employed singular coupling function $g(\eta)$ can be modified in order to obtain the desired misorientation dependence of the grain boundary energy without changing the variational form of the model; examples are Read-Shockley type or inclination dependent anisotropic energies.

While the HMP based model is a mathematically improved formulation compared to KWC, it is still highly non-linear and thus computationally heavy. Therefore, in this work we have shown the fundamental capabilities of the proposed model with simple numerical examples. In future work, inclination dependent grain boundaries, complex, plastic deformation induced microstructure evolution and sub-grain formation in polycrystals will be explored.

CRediT authorship contribution statement

I.T. Tandogan: Writing – original draft, Visualization, Validation, Software, Methodology, Investigation, Formal analysis, Data curation, Conceptualization. **M. Budnitzki:** Writing – review & editing, Validation, Supervision, Resources, Methodology, Formal analysis, Conceptualization. **S. Sandfeld:** Writing – review & editing, Supervision, Resources, Project administration, Funding acquisition.

Declaration of competing interest

The authors declare that they have no known competing financial interests or personal relationships that could have appeared to influence the work reported in this paper.

Acknowledgment

We are grateful to Dr. Anna Ask and Prof. Samuel Forest for their insight and valuable discussions.

Appendix A. Model parameters

At this initial stage of the model development, we are conducting qualitative tests and thus have not exactly fitted the parameters to experimental data. Nevertheless, the parameters are selected to be in an acceptable range for pure copper. For the mechanical part of the model, the elasticity constants for isotropic elasticity and cubic anisotropy are available in the literature [cf. Ledbetter and Naimon, 1974], and the values from Gérard et al. (2009) and Bacroix and Brenner (2012) are adapted for the plasticity and hardening. The Cosserat couple modulus μ_c is a penalty parameter preventing differences between Cosserat microrotation $\dot{\boldsymbol{\theta}}$ and lattice rotation $\overset{\times}{\underline{\omega}}$. Hence, it needs to be large enough, ideally some orders higher than elastic shear modulus μ^e. The parameters of the orientation phase field model α, ν and μ should be selected carefully so that the grain bulk and boundary are clearly distinguished while staying in the limitations of the model. These parameters determine the width, energy and the mobility of grain boundaries. For a grain boundary without inclination dependence, the 1D equilibrium profiles of order parameter η and orientation θ can be obtained with asymptotic analysis as outlined in Henry et al. (2012) and Staublin et al. (2022). However, we first need to non-dimensionalize our free energy functional.

A length scale L with unit m is defined, where $(\overline{x},\overline{y},\overline{z}) = (x,y,z)/L$ are dimensionless coordinates. With L we can non-dimensionalize the following parameters and differential operator

$$\overline{\alpha} = \alpha, \quad \overline{\nu} = \nu/L, \quad \overline{\mu} = \mu/L, \quad \overline{\nabla} = L\nabla, \quad \overline{C}_A = C_{\mathrm{A}}/L, \quad \overline{C}_* = C_*/L. \tag{A.1}$$

The mechanical parameters are non-dimensionalized using f_0 with unit Pa as

$$\overline{\underset{\approx}{E}}^{\mathrm{s}} = \underset{\approx}{E}^{\mathrm{s}}/f_0, \quad \overline{\mu}_{\mathrm{c}} = \mu_{\mathrm{c}}/f_0, \quad \overline{\lambda} = \lambda, \quad \overline{\mu}^{\mathrm{e}} = \mu^{\mathrm{e}}/f_0, \quad \overline{r}_\alpha = r_\alpha. \tag{A.2}$$

Finally, the non-dimensional free energy functional is given by

$$\begin{aligned}\overline{\psi} = \frac{\psi}{f_0} = &\left[\overline{\alpha}V(\eta) + \frac{\overline{\nu}^2}{2}|\overline{\nabla}\eta|^2 + \overline{\mu}^2 g(\eta)|\overline{\nabla}\theta|^2\right] \\ &+ \frac{1}{2}\underset{\sim}{\varepsilon}^{\mathrm{e}} : \overline{\underset{\approx}{E}}^{\mathrm{s}} : \underset{\sim}{\varepsilon}^{\mathrm{e}} + 2\overline{\mu}_{\mathrm{c}}\,\overset{\times}{e}{}^{\mathrm{e}\,2} + \phi(\eta)\sum_{\alpha=1}^{N}\frac{\overline{\lambda}}{2}\overline{\mu}^{\mathrm{e}}\overline{r}_\alpha^2.\end{aligned} \tag{A.3}$$

The dimensionless total energy can be calculated by

$$\overline{\Psi} = \frac{\Psi}{f_0 L^3} = \int_{\overline{\Omega}} \overline{\psi}\, d\overline{\Omega}, \tag{A.4}$$

where $d\overline{\Omega} = L^3 d\Omega$. By defining a time scale t_0 with $\overline{t} = t/t_0$, we can non-dimensionalize mobility constants

$$\overline{\tau}_\eta = \frac{\tau_\eta}{f_0 t_0}, \quad \overline{\tau}_* = \frac{\hat{\tau}_*}{f_0 t_0}. \tag{A.5}$$

The equilibrium profile between two semi-infinite grains with different lattice orientations can be found by considering Eqs. (44) and (46) without dislocations and setting the rates to zero,

$$0 = \nu^2\frac{\partial^2\eta}{\partial x^2} - \alpha V_{,\eta} + \mu^2 g_{,\eta}\left(\frac{\partial\theta}{\partial x}\right)^2, \tag{A.6}$$

$$0 = \frac{\partial}{\partial x}\cdot\left[g(\eta)\frac{\partial\theta}{\partial x}\right]. \tag{A.7}$$

These equations are solved by dividing the space into an inner region with rapid change of variables and an outer region where change is small. Then integration constants are found by equating the inner and outer region solutions at the intersection point. The field variables in the inner region are expanded in terms of a small constant ϵ as

$$\begin{aligned}\eta &= \eta^0 + \epsilon\frac{\partial\eta}{\partial x} + \epsilon^2\frac{\partial^2\eta}{\partial x^2} + \cdots \quad , \\ \theta &= \theta^0 + \epsilon\frac{\partial\theta}{\partial x} + \epsilon^2\frac{\partial^2\theta}{\partial x^2} + \cdots \quad .\end{aligned} \tag{A.8}$$

Here, we only provide the final forms and the reader is referred to Henry et al. (2012) and Staublin et al. (2022) for details. Leading order solutions are given by

$$\frac{\partial\theta^0}{\partial z} = \frac{A}{g(\eta^0)}, \tag{A.9}$$

$$\frac{\partial\eta^0}{\partial z} = \pm\frac{\sqrt{2}}{\overline{\nu}}\sqrt{\overline{\alpha}V(\eta^0) - \frac{A^2\overline{\mu}^2}{g(\eta^0)}}, \tag{A.10}$$

where $z = x/\epsilon$ is a stretched coordinate, A is a constant and (A.10) changes sign at the middle of the grain boundary. The dimensionless grain boundary energy $\tilde{\gamma}_{\mathrm{gb}}$ is given by

$$\tilde{\gamma}_{\mathrm{gb}}(\Delta\theta) = 2\sqrt{2}\overline{\nu}\int_{\eta^0_{\min}}^{1}\frac{\overline{\alpha}V(\eta^0)}{\sqrt{\overline{\alpha}V(\eta^0) - \frac{A^2\overline{\mu}^2}{g(\eta^0)}}}d\eta, \tag{A.11}$$

and the true grain boundary energy is

$$\gamma_{\mathrm{gb}} = f_0 L\epsilon\,\tilde{\gamma}_{\mathrm{gb}}. \tag{A.12}$$

To solve the preceding equations, one can start with an η^0 slightly smaller than 1, pick a value for the constant A and then solve (A.10) using finite differences. Then, using η^0 one can similarly calculate θ^0 with (A.9), which gives a certain misorientation $\Delta\theta$ depending on chosen value of A. Finally, $\tilde{\gamma}_{\mathrm{gb}}(\Delta\theta)$ for the given misorientation can be found with (A.11).

Fig. A.18 shows an example of equilibrium profiles for different misorientations obtained from asymptotic analysis with parameters $\overline{\alpha} = 150$, $\overline{\nu} = 1$, $\overline{\mu} = 2.5/\pi$ and $\epsilon = 1$. When $\overline{\nu}$ is kept constant, increasing $\overline{\alpha}$ results in a thinner grain boundary, and increasing $\overline{\mu}$ gives a deeper profile of η^0. It is important to have a sufficiently large $\overline{\mu}$ so that the η profile is not too shallow for small misorientations.

For the mesoscale, an appropriate length scale is $L = 1\,\mu\mathrm{m}$. A property of the HMP and KWC phase field models is the existence of two grain boundary dimensions for η and θ, which are about $1\,\mu\mathrm{m}$ and $0.4\,\mu\mathrm{m}$, respectively, (see Fig. A.18) in our examples. In the case of instantaneous response during mechanical loading the latter is more important since it determines the local stress, and

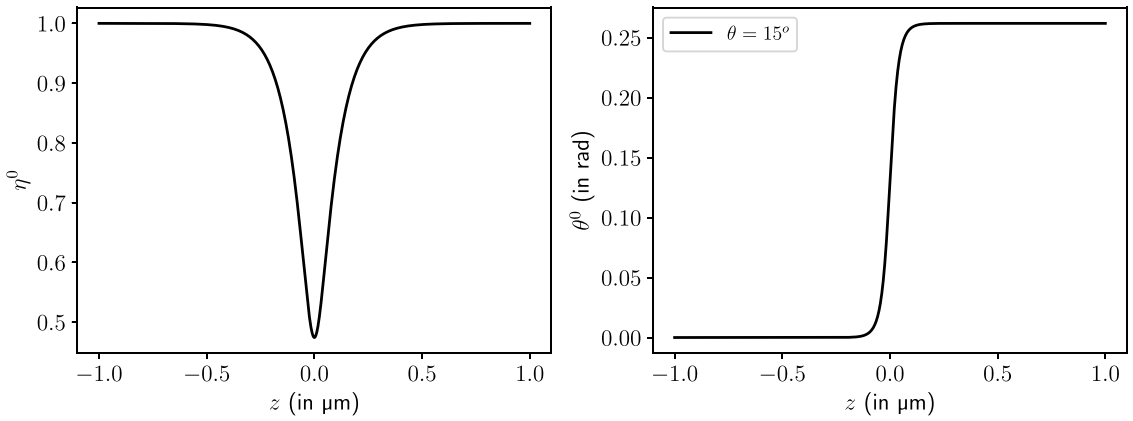

Fig. A.18. Equilibrium profiles of order parameter and orientation field for given misorientation found from asymptotic analysis with parameters $\overline{\alpha} = 150$, $\overline{\nu} = 1$, $\overline{\mu} = 2.5/\pi$ and $\epsilon = 1$.

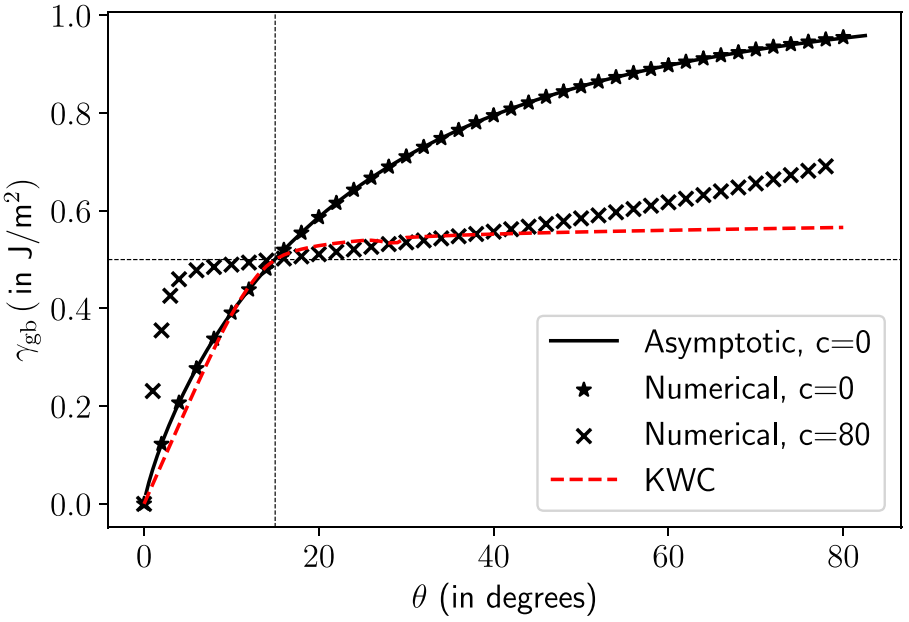

Fig. A.19. Grain boundary energies at increasing misorientations calibrated to an approximate 0.5 J/m^2 at 15° misorientation for pure Copper. The curves correspond to: the solid line and star markers using $g(\eta)$, the cross markers where $g(\eta)$ is replaced with $g(\eta) + c\log(1-\eta) + C_0$ to generate a Read-Shockley type grain boundary energy, and the dashed line for the KWC model. The values of f_0 are 87 kJ/m^3, 313.6 kJ/m^3 and 5765.4 kJ/m^3, respectively. The parameters for KWC in Eq. (49) are $\nu = 0.09$ μm, $s = 0.4$ μm and $\epsilon = 0.8$ μm.

it is in acceptable range for diffuse grain boundary models. It is also possible to reduce the difference by changing the free energy contributions (Ghiglione et al., 2024).

Using Eqs. (A.11) and (A.12), the model parameters can be calibrated to fit experimental grain boundary energy data. In this work, we do not pursue a rigorous fitting. Instead, we assume an average grain boundary energy of 0.5 J/m^2 at 15 degrees misorientation for copper, which is in an acceptable range (Tschopp et al., 2015). Using Eq. (A.12), this gives $f_0 = 87$ kJ/m^3. The resulting grain boundary energy up to 80 degrees of misorientation is shown in Fig. A.19 with black solid line. The markers show the energy calculated numerically with the finite element method, and there is excellent agreement with the asymptotic analysis.

A feature of the HMP-type orientation phase field is that, if the singularity at $g(1)$ is preserved, arbitrary functions can be added to $g(\eta)$ to modify the dependency of grain boundary energy on misorientation without changing the free energy or evolution equations; for example, inclination dependence (Henry et al., 2012) can be incorporated. Similarly, a Read-Shockley type grain boundary energy

can be obtained by making a small modification to the singular function $g(\eta)$, i.e.,

$$g(\eta) = \frac{7\eta^3 - 6\eta^4}{(1-\eta)^3} + c\ln(1-\eta) + C_0 \quad \text{where} \quad C_0 = \min\left(\frac{7\eta_*^3 - 6\eta_*^4}{(1-\eta_*)^3} + c\ln(1-\eta_*)\right) + 0.01, \tag{A.13}$$

and η_* take values in range [0,1] (see Staublin et al., 2022 for details). The resulting curve with $c = 80$ is plotted in Fig. A.19.

For comparison the KWC orientation phase field model's grain boundary energy, numerically calculated from Eq. (49), is also plotted in Fig. A.19. It is fitted to have 0.5 J/m^2 at 15°, and similar energies compared to HMP (with $c = 0$) between 10°–15°, which is the range of angles used in Section 3.5.

The proposed coupled Cosserat model and the pure HMP phase field have the same equilibrium condition, meaning the leading order solutions from the asymptotic analysis of HMP can be used for both models to obtain equilibrium profiles and the grain boundary energy. However, the next to leading order solution of grain boundary mobility presented in Staublin et al. (2022) is no longer valid for the coupled Cosserat model, because the orientation update is based on balance Eq. (45) and constraint (39), instead of relaxation dynamics. In addition, the coupled model has an additional driving force for grain boundaries due to stored dislocations. Still, as discussed in Ask et al. (2020), it is possible to estimate the grain boundary mobility by relying on simple numerical test cases.

Appendix B. Analytic solution for elastic shear loading of the periodic bicrystal

Here a summary of the equations of the analytic solution to elastic shear loading of a periodic bicrystal with cubic anisotropy is presented. For the derivation and details please refer to Ask et al. (2018a).

Loading is applied by imposing a mean displacement field with periodic fluctuations. The total displacement $\underline{\boldsymbol{u}}$ is given by

$$\underline{\boldsymbol{u}} = \underset{\sim}{\boldsymbol{B}} \cdot \underline{\boldsymbol{x}} + \underline{\boldsymbol{v}}, \tag{B.1}$$

where $\underline{\boldsymbol{x}}$ is spatial coordinates, $\underline{\boldsymbol{v}}$ is the periodic fluctuation vector and $\underset{\sim}{\boldsymbol{B}} \cdot \underline{\boldsymbol{x}}$ is mean displacement field. The tensor $\underset{\sim}{\boldsymbol{B}}$ is defined as

$$\underset{\sim}{\boldsymbol{B}} = \begin{bmatrix} 0 & B_{12} & 0 \\ B_{21} & 0 & 0 \\ 0 & 0 & 0 \end{bmatrix} \tag{B.2}$$

for shear loading. For simple shear either B_{12} or B_{21} is zero. Assuming $B_{12} = 0$, displacements are given by,

$$\begin{aligned} u_1 &= v_1(x_1), \\ u_2 &= B_{21}x_1 + v_2(x_1), \\ u_3 &= 0. \end{aligned} \tag{B.3}$$

Assuming small deformations and plane strain conditions, the only non-zero strains are

$$\varepsilon_{11} = \frac{\partial v_1}{\partial x_1}, \qquad \varepsilon_{12} = \varepsilon_{21} = \frac{1}{2}\left(B_{21} + \frac{\partial v_2}{\partial x_1}\right). \tag{B.4}$$

Assuming cubic elasticity, the stiffness tensor and the compliance tensor can be defined with three independent constants each: C_{11}, C_{12} and C_{44}, or S_{11}, S_{12} and S_{44}, respectively. We have the following relations between them:

$$S_{11} = \frac{C_{11} + C_{12}}{(C_{11} + 2C_{12})(C_{11} - C_{12})}, \qquad S_{12} = \frac{-C_{12}}{(C_{11} + 2C_{12})(C_{11} - C_{12})}, \qquad S_{44} = \frac{1}{C_{44}}. \tag{B.5}$$

Assume that we have a varying orientation field θ along x_1 direction. The constitutive relation is applied at the material frame and then θ is used to obtain strains in the global frame in terms of stresses. Then enforcing constraints (B.4) results in a system of equations with unknown stresses σ_{12}, σ_{11} and σ_{22}. After solving the system, σ_{33} is found from plane strain conditions. We get

$$\sigma_{12} = \frac{1}{2F}B_{21}, \qquad \sigma_{11} = E\sigma_{12}, \qquad \sigma_{22} = -\frac{B}{A}\sigma_{11} - \frac{C}{A}\sigma_{12}, \qquad \sigma_{33} = -\frac{S_{12}}{S_{11}}(\sigma_{11} + \sigma_{22}), \tag{B.6}$$

where the orientation dependent coefficients are given by

$$E = \frac{\langle C/A \rangle}{1 - \langle B/A \rangle}, \qquad F = \left\langle -\frac{C + CE}{2} - \frac{CEB + C^2}{2A} + D \right\rangle. \tag{B.7}$$

In this case $\langle\cdot\rangle$ represent the average and

$$\begin{aligned} A &= S_{11} + S_D + S_A\sin^2(2\theta), \quad B = S_{12} + S_D - S_A\sin^2(2\theta), \\ C &= S_A\sin(4\theta), \quad D = S_B + S_A\cos(4\theta), \\ S_A &= \frac{1}{2}\left(-S_{11} + S_{12} + \frac{1}{2}S_{44}\right), \quad S_B = \frac{1}{2}\left(S_{11} - S_{12} + \frac{1}{2}S_{44}\right), \quad S_D = -\frac{S_{12}^2}{S_{11}}. \end{aligned} \tag{B.8}$$

An orientation field in the form

$$\theta = \frac{\pi}{24}\left[\tanh(c[\overline{x} + \overline{x}_{\text{shift}}]) + 1\right] \tag{B.9}$$

gives a change from 0 to 15 degrees around position $\overline{x}_{\text{shift}}$ with varying sharpness determined by the parameter c. Fig. B.20 shows the stresses obtained using elasticity parameters in Table 1 and Eq. (B.9).

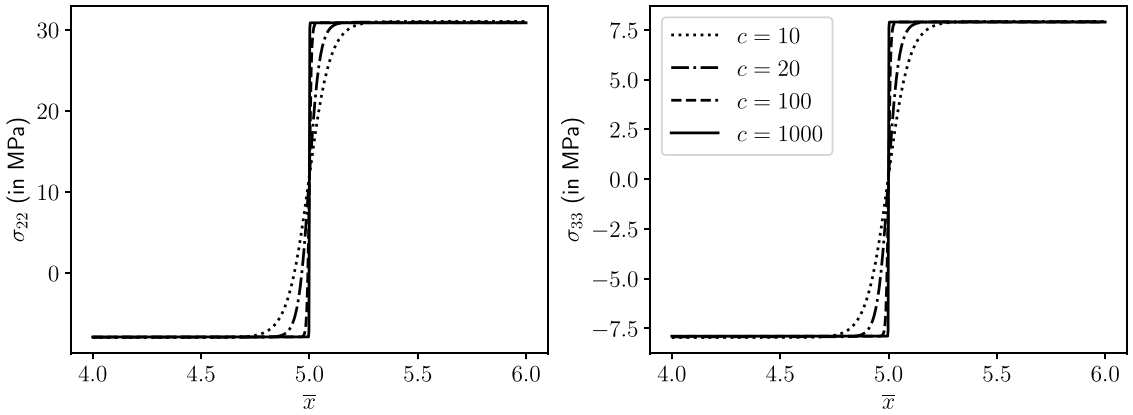

Fig. B.20. Stress profiles across the grain boundary with changing orientation with different sharpness.

Appendix C. 2D numerical implementation in FEniCS

The model is implemented in the FEniCS 2019 open-source finite element library (Alnaes et al., 2015) and the MFront code generator for the material models (Helfer et al., 2015). After the simplifications in Section 2.3, for a single slip system, the strong form equations are given by

$$\tau_\eta \dot{\eta} = f_0 \nu^2 \nabla^2 \eta - f_0 \left[\alpha V_{,\eta} + \mu^2 g_{,\eta} |\nabla\theta|^2\right] - \phi_{,\eta}\psi_\rho, \tag{C.1}$$

$$0 = f_0 \nabla \cdot \left[\mu^2 g(\eta) \nabla\theta\right] + \overset{\times}{\sigma}, \tag{C.2}$$

$$\underline{\mathbf{0}} = \nabla \cdot \underset{\sim}{\sigma}, \tag{C.3}$$

where

$$V(\eta) = \frac{1}{2}(1-\eta)^2, \qquad g(\eta) = \frac{7\eta^3 - 6\eta^4}{(1-\eta)^3}, \qquad \phi(\eta) = -2\eta^4 + 3\eta^3 - \eta^2 + \eta, \qquad \psi_\rho = \frac{\lambda}{2}\mu^e b^2 \rho. \tag{C.4}$$

The weak form is obtained by multiplying the strong forms with test functions w_η, w_θ, $\underline{\boldsymbol{w}}_u$ and integrating. We get,

$$\int_\Omega \left\{ f_0 \nu^2 \nabla\eta \cdot \nabla w_\eta + \left(\tau_\eta \dot{\eta} + f_0 \left[\alpha V_{,\eta} + \mu^2 g_{,\eta} |\nabla\theta|^2 \right] + \phi_{,\eta}\psi_\rho \right) w_\eta \right\} dV = \int_{\partial\Omega} f_0 \nu^2 \nabla\eta \cdot \underline{\boldsymbol{n}}\, w_\eta dS, \tag{C.5}$$

$$\int_\Omega \left\{ f_0 \mu^2 g(\eta) \nabla\theta \cdot \nabla w_\theta - \overset{\times}{\sigma} w_\theta \right\} dV = \int_{\partial\Omega} f_0 \mu^2 g(\eta) \nabla\theta \cdot \underline{\boldsymbol{n}}\, w_\theta dS, \tag{C.6}$$

$$\int_\Omega \left\{ \underset{\sim}{\boldsymbol{\sigma}}^s(\underline{\boldsymbol{u}}) : \underset{\sim}{\boldsymbol{\varepsilon}}(\underline{\boldsymbol{w}}_u) + 2\overset{\times}{\underset{\sim}{\boldsymbol{\sigma}}}(\underline{\boldsymbol{u}}) \cdot \overset{\times}{\underset{\sim}{\boldsymbol{\omega}}}(\underline{\boldsymbol{w}}_u) \right\} = \int_{\partial\Omega} (\underset{\sim}{\boldsymbol{\sigma}} \cdot \underline{\boldsymbol{n}}) \cdot \underline{\boldsymbol{w}}_u dS. \tag{C.7}$$

The equations are discretized in time implicitly, except for the highlighted term in (C.5) where the value in the beginning of the increment is used. The state variables are updated with the following equations

$$\Delta \overset{\times}{\underline{\boldsymbol{e}}}^* = \frac{\frac{\Delta t 2\mu_c}{\hat{\tau}_* g(\eta)} \left(\overset{\times}{\underline{\boldsymbol{e}}} - \overset{\times}{\underline{\boldsymbol{e}}}^*_n - \overset{\times}{\underline{\boldsymbol{e}}}^{\text{slip}} \right)}{1 + \frac{\Delta t 2\mu_c}{\hat{\tau}_* g(\eta)}}, \tag{C.8}$$

$$\Delta \rho_{\text{recovery}} = \begin{cases} -\rho C_D \tanh(C_A^2 |\nabla\theta_n|^2) \Delta\eta & \text{if} \quad \Delta\eta > 0, \\ 0 & \text{if} \quad \Delta\eta \le 0, \end{cases} \tag{C.9}$$

The system of nonlinear equations are solved monolithically using the Newton–Raphson procedure. During the iterations, due to the singular nature of $g(\eta)$, the residual from Eq. (C.6) is significantly larger than the residual from (C.5). Therefore, in order to solve these equations monolithically, the former is normalized with a coefficient of 10^{-10}. Moreover, to increase the numerical stability, the singular function $g(\eta)$ is modified with a cut-off value as follows

$$g(\eta) \to g(\min(\eta, \eta_{\text{cutoff}})), \tag{C.10}$$

where η_{cutoff} was taken as $(1 - 10^{-4})$ or $(1 - 10^{-5})$.

Data availability

Data will be made available on request.

References

Abrivard, G., Busso, E.P., Forest, S., Appolaire, B., 2012. Phase field modelling of grain boundary motion driven by curvature and stored energy gradients. Part I: theory and numerical implementation. Phil. Mag. 92 (28–30), 3618–3642.

Admal, N.C., Po, G., Marian, J., 2018. A unified framework for polycrystal plasticity with grain boundary evolution. Int. J. Plast. 106, 1–30.

Admal, N.C., Segurado, J., Marian, J., 2019. A three-dimensional misorientation axis-and inclination-dependent Kobayashi–Warren–Carter grain boundary model. J. Mech. Phys. Solids 128, 32–53.

Alnaes, M., Blechta, J., Hake, J., Johansson, A., Kehlet, B., Logg, A., Richardson, C., Ring, J., Rognes, M.E., Wells, G.N., 2015. The FEniCS project version 1.5. Arch. Numer. Softw. 3 (100).

Asaro, R.J., Rice, J., 1977. Strain localization in ductile single crystals. J. Mech. Phys. Solids 25 (5), 309–338.

Ashby, M., 1970. The deformation of plastically non-homogeneous materials. Philos. Mag. J. Theor. Exp. Appl. Phys. 21 (170), 399–424.

Ask, A., Forest, S., Appolaire, B., Ammar, K., 2018b. Cosserat crystal plasticity with dislocation-driven grain boundary migration. J. Micromech. Mol. Phys. 3 (03n04), 1840009.

Ask, A., Forest, S., Appolaire, B., Ammar, K., 2019. A Cosserat–phase-field theory of crystal plasticity and grain boundary migration at finite deformation. Contin. Mech. Thermodyn. 31, 1109–1141.

Ask, A., Forest, S., Appolaire, B., Ammar, K., 2020. Microstructure evolution in deformed polycrystals predicted by a diffuse interface Cosserat approach. Adv. Model. Simul. Eng. Sci. 7 (1), 1–28.

Ask, A., Forest, S., Appolaire, B., Ammar, K., Salman, O.U., 2018a. A cosserat crystal plasticity and phase field theory for grain boundary migration. J. Mech. Phys. Solids 115, 167–194.

Bacroix, B., Brenner, R., 2012. A phenomenological anisotropic description for dislocation storage and recovery processes in fcc crystals. Comput. Mater. Sci. 54, 97–100.

Baek, J., Chen, J.S., Tupek, M., Beckwith, F., Fang, H.E., 2022. A duality-based coupling of Cosserat crystal plasticity and phase field theories for modeling grain refinement. Internat. J. Numer. Methods Engrg. 123 (4), 953–991.

Bailey, J., Hirsch, P.B., 1962. The recrystallization process in some polycrystalline metals. Proc. R. Soc. A 267 (1328), 11–30.

Basak, A., Gupta, A., 2015. Simultaneous grain boundary motion, grain rotation, and sliding in a tricrystal. Mech. Mater. 90, 229–242.

Berbenni, S., Paliwal, B., Cherkaoui, M., 2013. A micromechanics-based model for shear-coupled grain boundary migration in bicrystals. Int. J. Plast. 44, 68–94.

Bernacki, M., Chastel, Y., Coupez, T., Logé, R.E., 2008. Level set framework for the numerical modelling of primary recrystallization in polycrystalline materials. Scr. Mater. 58 (12), 1129–1132.

Bernacki, M., Logé, R.E., Coupez, T., 2011. Level set framework for the finite-element modelling of recrystallization and grain growth in polycrystalline materials. Scr. Mater. 64 (6), 525–528.

Blesgen, T., 2014. Deformation patterning in three-dimensional large-strain Cosserat plasticity. Mech. Res. Commun. 62, 37–43.

Blesgen, T., 2017. A variational model for dynamic recrystallization based on Cosserat plasticity. Composites B 115, 236–243.

Bugas, D., Runnels, B., 2024. Grain boundary network plasticity: Reduced-order modeling of deformation-driven shear-coupled microstructure evolution. J. Mech. Phys. Solids 184, 105541.

Cahn, J.W., Mishin, Y., Suzuki, A., 2006. Coupling grain boundary motion to shear deformation. Acta Mater. 54 (19), 4953–4975.

Cailletaud, G., 1992. A micromechanical approach to inelastic behaviour of metals. Int. J. Plast. 8 (1), 55–73.

Chen, L.Q., 1995. A novel computer simulation for modeling grain growth. Scr. Metall. Mater.;(United States) 32 (1).

Chen, L., Chen, J., Lebensohn, R., Ji, Y., Heo, T., Bhattacharyya, S., Chang, K., Mathaudhu, S., Liu, Z., Chen, L.-Q., 2015. An integrated fast Fourier transform-based phase-field and crystal plasticity approach to model recrystallization of three dimensional polycrystals. Comput. Methods Appl. Mech. Engrg. 285, 829–848.

Chen, Y., Han, J., Deng, H., Cao, G., Zhang, Z., Zhu, Q., Zhou, H., Srolovitz, D.J., Wang, J., 2024. Revealing grain boundary kinetics in three-dimensional space. Acta Mater. 268, 119717.

Eringen, A.C., Kafadar, C.B., 1976. Polar field theories. In: Continuum Physics. Elsevier, pp. 1–73.

Fan, D., Chen, L.Q., 1997. Computer simulation of grain growth using a continuum field model. Acta Mater. 45 (2), 611–622.

Forest, S., 2008. Some links between Cosserat, strain gradient crystal plasticity and the statistical theory of dislocations. Phil. Mag. 88 (30–32), 3549–3563.

Forest, S., Barbe, F., Cailletaud, G., 2000. Cosserat modelling of size effects in the mechanical behaviour of polycrystals and multi-phase materials. Int. J. Solids Struct. 37 (46–47), 7105–7126.

Forest, S., Ghiglione, F., 2023. Size effects in Cosserat crystal plasticity. In: Sixty Shades of Generalized Continua: Dedicated to the 60th Birthday of Prof. Victor A. Eremeyev. Springer, pp. 211–234.

Gérard, C., Bacroix, B., Bornert, M., Cailletaud, G., Crépin, J., Leclercq, S., 2009. Hardening description for FCC materials under complex loading paths. Comput. Mater. Sci. 45 (3), 751–755.

Ghiglione, F., Ask, A., Ammar, K., Appolaire, B., Forest, S., 2024. Cosserat-phase-field modeling of grain nucleation in plastically deformed single crystals. J. Mech. Phys. Solids 105628.

Gill, S., Cocks, A., 1996. A variational approach to two dimensional grain growth—II. Numerical results. Acta Mater. 44 (12), 4777–4789.

Gottstein, G., Shvindlerman, L.S., 2009. Grain Boundary Migration in Metals: Thermodynamics, Kinetics, Applications. CRC Press.

Gurtin, M.E., 1996. Generalized Ginzburg–Landau and Cahn–Hilliard equations based on a microforce balance. Physica D 92 (3–4), 178–192.

Gurtin, M.E., 2000. On the plasticity of single crystals: free energy, microforces, plastic-strain gradients. J. Mech. Phys. Solids 48 (5), 989–1036.

Gurtin, M.E., 2008. A finite-deformation, gradient theory of single-crystal plasticity with free energy dependent on densities of geometrically necessary dislocations. Int. J. Plast. 24 (4), 702–725.

He, J., Admal, N.C., 2021. Polycrystal plasticity with grain boundary evolution: A numerically efficient dislocation-based diffuse-interface model. Modelling Simul. Mater. Sci. Eng. 30 (2), 025006.

Helfer, T., Bleyer, J., Frondelius, T., Yashchuk, I., Nagel, T., Naumov, D., 2020. The MFrontGenericInterfaceSupport project. J. Open Source Softw. 5 (48), 1–8.

Helfer, T., Michel, B., Proix, J.M., Salvo, M., Sercombe, J., Casella, M., 2015. Introducing the open-source mfront code generator: Application to mechanical behaviours and material knowledge management within the PLEIADES fuel element modelling platform. Comput. Math. Appl. 70 (5), 994–1023.

Henry, H., Mellenthin, J., Plapp, M., 2012. Orientation-field model for polycrystalline solidification with a singular coupling between order and orientation. Phys. Rev. B 86 (5), 054117.

Herring, C., 1951. Some theorems on the free energies of crystal surfaces. Phys. Rev. 82 (1), 87.

Hirth, J.P., Lothe, J., Mura, T., 1983. Theory of dislocations. J. Appl. Mech. 50 (2), 476–477.

Hu, X., Ji, Y., Chen, L., Lebensohn, R.A., Chen, L.Q., Cui, X., 2021. Spectral phase-field model of deformation twinning and plastic deformation. Int. J. Plast. 143, 103019.

Joshi, H., He, J., Admal, N.C., 2022. A finite deformation theory for grain boundary plasticity based on geometrically necessary disconnections. J. Mech. Phys. Solids 167, 104949.

Kim, J., Jacobs, M., Osher, S., Admal, N.C., 2021. A crystal symmetry-invariant Kobayashi–Warren–Carter grain boundary model and its implementation using a thresholding algorithm. Comput. Mater. Sci. 199, 110575.

Kobayashi, R., Giga, Y., 1999. Equations with singular diffusivity. J. Stat. Phys. 95, 1187–1220.

Kobayashi, R., Warren, J.A., Carter, W.C., 2000. A continuum model of grain boundaries. Physica D 140 (1–2), 141–150.
Korbuly, B., Plapp, M., Henry, H., Warren, J.A., Gránásy, L., Pusztai, T., 2017. Topological defects in two-dimensional orientation-field models for grain growth. Phys. Rev. E 96 (5), 052802.
Ledbetter, H., Naimon, E., 1974. Elastic properties of metals and alloys. II. Copper. J. Phys. Chem. Ref. Data 3 (4), 897–935.
Li, H., Sun, X., Yang, H., 2016. A three-dimensional cellular automata-crystal plasticity finite element model for predicting the multiscale interaction among heterogeneous deformation, DRX microstructural evolution and mechanical responses in titanium alloys. Int. J. Plast. 87, 154–180.
Luan, Q., Lee, J., Zheng, J.H., Hopper, C., Jiang, J., 2020. Combining microstructural characterization with crystal plasticity and phase-field modelling for the study of static recrystallization in pure aluminium. Comput. Mater. Sci. 173, 109419.
Marano, A., Gélébart, L., Forest, S., 2019. Intragranular localization induced by softening crystal plasticity: Analysis of slip and kink bands localization modes from high resolution FFT-simulations results. Acta Mater. 175, 262–275.
Marx, V., Reher, F., Gottstein, G., 1999. Simulation of primary recrystallization using a modified three-dimensional cellular automaton. Acta Mater. 47 (4), 1219–1230.
Mayeur, J., McDowell, D., 2014. A comparison of Gurtin type and micropolar theories of generalized single crystal plasticity. Int. J. Plast. 57, 29–51.
Mayeur, J.R., McDowell, D.L., Bammann, D.J., 2011. Dislocation-based micropolar single crystal plasticity: Comparison of multi-and single criterion theories. J. Mech. Phys. Solids 59 (2), 398–422.
McElfresh, C., Marian, J., 2023. Initial grain orientation controls static recrystallization outcomes in cold-worked iron: Insight from coupled crystal plasticity/vertex dynamics modeling. Acta Mater. 245, 118631.
Mikula, J., Joshi, S.P., Tay, T.E., Ahluwalia, R., Quek, S.S., 2019. A phase field model of grain boundary migration and grain rotation under elasto–plastic anisotropies. Int. J. Solids Struct. 178, 1–18.
Mishin, Y., Asta, M., Li, J., 2010. Atomistic modeling of interfaces and their impact on microstructure and properties. Acta Mater. 58 (4), 1117–1151.
Nagra, J.S., Brahme, A., Lévesque, J., Mishra, R., Lebensohn, R.A., Inal, K., 2020. A new micromechanics based full field numerical framework to simulate the effects of dynamic recrystallization on the formability of HCP metals. Int. J. Plast. 125, 210–234.
Popova, E., Staraselski, Y., Brahme, A., Mishra, R., Inal, K., 2015. Coupled crystal plasticity–Probabilistic cellular automata approach to model dynamic recrystallization in magnesium alloys. Int. J. Plast. 66, 85–102.
Raabe, D., 2002. Cellular automata in materials science with particular reference to recrystallization simulation. Annu. Rev. Mater. Res. 32 (1), 53–76.
Rollett, A., Luton, M., Srolovitz, D.J., 1992. Microstructural simulation of dynamic recrystallization. Acta Metall. Mater. 40 (1), 43–55.
Rollett, A., Rohrer, G.S., Humphreys, J., 2017. Recrystallization and Related Annealing Phenomena. Newnes.
Roters, F., Eisenlohr, P., Hantcherli, L., Tjahjanto, D.D., Bieler, T.R., Raabe, D., 2010. Overview of constitutive laws, kinematics, homogenization and multiscale methods in crystal plasticity finite-element modeling: Theory, experiments, applications. Acta Mater. 58 (4), 1152–1211.
Ryś, M., Stupkiewicz, S., Petryk, H., 2022. Micropolar regularization of crystal plasticity with the gradient-enhanced incremental hardening law. Int. J. Plast. 156, 103355.
Sarrazola, D.R., Maire, L., Moussa, C., Bozzolo, N., Muñoz, D.P., Bernacki, M., 2020a. Full field modeling of dynamic recrystallization in a CPFEM context–Application to 304L steel. Comput. Mater. Sci. 184, 109892.
Sarrazola, D.R., Muñoz, D.P., Bernacki, M., 2020b. A new numerical framework for the full field modeling of dynamic recrystallization in a CPFEM context. Comput. Mater. Sci. 179, 109645.
Sedláček, R., Blum, W., Kratochvil, J., Forest, S., 2002. Subgrain formation during deformation: physical origin and consequences. Metall. Mater. Trans. A 33, 319–327.
Sitko, M., Chao, Q., Wang, J., Perzynski, K., Muszka, K., Madej, L., 2020. A parallel version of the cellular automata static recrystallization model dedicated for high performance computing platforms–Development and verification. Comput. Mater. Sci. 172, 109283.
Soares, A., Ferro, A., Fortes, M., 1985. Computer simulation of grain growth in a bidimensional polycrystal. Scr. Metall. 19 (12), 1491–1496.
Srolovitz, D., 1986. Grain growth phenomena in films: A Monte Carlo approach. J. Vac. Sci. Technol. A 4 (6), 2925–2931.
Staublin, P., Mukherjee, A., Warren, J.A., Voorhees, P.W., 2022. Phase-field model for anisotropic grain growth. Acta Mater. 237, 118169.
Steinbach, I., Pezzolla, F., 1999. A generalized field method for multiphase transformations using interface fields. Physica D 134 (4), 385–393.
Steinbach, I., Pezzolla, F., Nestler, B., Seeßelberg, M., Prieler, R., Schmitz, G.J., Rezende, J.L., 1996. A phase field concept for multiphase systems. Physica D 94 (3), 135–147.
Sun, X.Y., Fressengeas, C., Taupin, V., Cordier, P., Combe, N., 2018. Disconnections, dislocations and generalized disclinations in grain boundary ledges. Int. J. Plast. 104, 134–146.
Sun, X.Y., Taupin, V., Fressengeas, C., Cordier, P., 2016. Continuous description of the atomic structure of grain boundaries using dislocation and generalized-disclination density fields. Int. J. Plast. 77, 75–89.
Takaki, T., Hisakuni, Y., Hirouchi, T., Yamanaka, A., Tomita, Y., 2009. Multi-phase-field simulations for dynamic recrystallization. Comput. Mater. Sci. 45 (4), 881–888.
Takaki, T., Tomita, Y., 2010. Static recrystallization simulations starting from predicted deformation microstructure by coupling multi-phase-field method and finite element method based on crystal plasticity. Int. J. Mech. Sci. 52 (2), 320–328.
Takaki, T., Yoshimoto, C., Yamanaka, A., Tomita, Y., 2014. Multiscale modeling of hot-working with dynamic recrystallization by coupling microstructure evolution and macroscopic mechanical behavior. Int. J. Plast. 52, 105–116.
Tourret, D., Liu, H., LLorca, J., 2022. Phase-field modeling of microstructure evolution: Recent applications, perspectives and challenges. Prog. Mater. Sci. 123, 100810.
Tschopp, M.A., Coleman, S.P., McDowell, D.L., 2015. Symmetric and asymmetric tilt grain boundary structure and energy in Cu and Al (and transferability to other fcc metals). Integr. Mater. Manuf. Innov. 4, 176–189.
Warren, J.A., Kobayashi, R., Lobkovsky, A.E., Carter, W.C., 2003. Extending phase field models of solidification to polycrystalline materials. Acta Mater. 51 (20), 6035–6058.
Yalçinkaya, T., Tandoğan, İ.T., Özdemir, İ., 2021. Void growth based inter-granular ductile fracture in strain gradient polycrystalline plasticity. Int. J. Plast. 147, 103123.
Zhao, P., Low, T.S.E., Wang, Y., Niezgoda, S.R., 2016. An integrated full-field model of concurrent plastic deformation and microstructure evolution: Application to 3D simulation of dynamic recrystallization in polycrystalline copper. Int. J. Plast. 80, 38–55.
Zhu, Q., Zhao, S., Deng, C., An, X., Song, K., Mao, S., Wang, J., 2020. In situ atomistic observation of grain boundary migration subjected to defect interaction. Acta Mater. 199, 42–52.